

**CERIUM PROMOTED NI/MGO CATALYST FOR
BIOGAS DRY REFORMING**

TEE CHIN CHOW

**BACHELOR OF CHEMICAL ENGINEERING UNIVERSITI MALAYSIA
PAHANG**

©TEE CHIN CHOW

Thesis Access Form

No _____ Location _____

Author:

Title :

Status of access OPEN / RESTRICTED / CONFIDENTIAL

Moratorium period: _____ years, ending _____ / _____ 200 _____

Conditions of access proved by (CAPITALS): DR CHENG CHIN KUI

Supervisor (Signature).....

Faculty:

Author's Declaration: *I agree the following conditions:*

OPEN access work shall be made available (in the University and externally) and reproduced as necessary at the discretion of the University Librarian or Head of Department. It may also be copied by the British Library in microfilm or other form for supply to requesting libraries or individuals, subject to an indication of intended use for non-publishing purposes in the following form, placed on the copy and on any covering document or label.

The statement itself shall apply to ALL copies:

This copy has been supplied on the understanding that it is copyright material and that no quotation from the thesis may be published without proper acknowledgement.

Restricted/confidential work: All access and any photocopying shall be strictly subject to written permission from the University Head of Department and any external sponsor, if any.

Author's signature.....**Date:**

users declaration: for signature during any Moratorium period (Not Open work):

I undertake to uphold the above conditions:

Date	Name (CAPITALS)	Signature	Address

CERIUM PROMOTED NI/MGO CATALYST FOR BIOGAS DRY REFORMING

TEE CHIN CHOW

Thesis submitted in partial fulfillment of the requirements
for the award of the degree of
Bachelor of Chemical Engineering

**Faculty of Chemical & Natural Resources Engineering
UNIVERSITI MALAYSIA PAHANG**

MAY 2014

©TEE CHIN CHOW (2014)

SUPERVISOR'S DECLARATION

We hereby declare that we have checked this thesis and in my opinion, this thesis is adequate in terms of scope and quality for the award of the degree of Bachelor of Chemical Engineering.

Signature :

Name of main supervisor : DR. CHENG CHIN KUI

Position : SENIOR LECTURER

Date : 25 MAY 2014

STUDENT'S DECLARATION

I declare that this thesis entitled 'Cerium-promoted Ni/MgO Catalyst for Biogas Dry Reforming' is the result of my own research except as cited in references. The thesis has not been accepted for any degree and is not concurrently submitted in candidature of any other degree.

Signature :
Name : TEE CHIN CHOW
ID Number : KA10016
Date : FEBRUARY 2014

Dedication

Special Dedication of This Appreciative Feeling to My...

Family, Lecturer and Friends

For Their Assistance, Encouragement and Wishes

ACKNOWLEDGEMENT

I wish to convey my hearty appreciation to my supervisor, Dr. Cheng Chin Kui for his opinion, advices, motivation, friendship, endless support, guidance and encouragement throughout the Undergraduate Research Project. I also feel thankful to my family and friends for their assistance and motivation in the thesis progress. Without their help, I may not be able to complete my thesis. I am also impressed to University Malaysia Pahang (UMP) for supplying the facilities for my research.

Finally, I am beholden to everybody that assisted me directly or indirectly in completing this thesis.

ABSTARCT

In the present work, different loadings of cerium promoted Ni/MgO catalyst for the biogas dry reforming reaction was studied. XRD diffraction pattern of fresh 5 wt% Ce-Ni/MgO catalyst showed peaks representing MgO at $2\theta = 37.00^\circ$ and NiO at 42.99° , 62.41° , 74.84° and 78.79° . BET characterization of both fresh 3 wt% and 5 wt% Ce-Ni/MgO catalysts presented that 5 wt% Ce-Ni/MgO catalyst has larger BET specific surface area, pore volume and pore diameter than 3 wt% Ce-Ni/MgO catalyst. From FESEM imaging of 5 wt% Ce-Ni/MgO catalyst, it can be observed that the metallic particles in the catalyst are uniformly distributed. EDX of fresh 5 wt% Ce-Ni/MgO catalyst displayed that only a small amount of carbon is found for the catalyst showing that the catalyst has high carbon removal efficiency. Reaction studies have found that both 3 wt% and 5 wt% Ce-Ni/MgO catalysts gave almost equal rate of formation of product yield (H_2 and CO) which is greater than that of unpromoted Ni/MgO catalyst. However, 5 wt% Ce-Ni/MgO catalyst gives a slightly higher conversion than 3wt% Ce-Ni/MgO catalyst indicating that 5 wt% Ce-Ni/MgO is the best performing catalyst. It was then employed for further reaction studies. The increasing temperature results in increase rate of formation of both CO and H_2 as well as the rate of CH_4 consumption in agreement with Arrhenius principle. CH_4 consumption showed the highest activation energy which is 62.59 kJ/kmol.

ABSTRAK

Kajian ini menyelidik tentang kandungan Ce yang berlainan dalam pemangkin Ni/MgO terhadap tindak balas metana dan karbon monoksida. Corak pembelauan XRD menunjukkan puncak yang mewakili MgO pada $2\theta = 37.00^\circ$ and NiO pada 42.99° , 62.41° , 74.84° and 78.79° . Pencirian BET bagi pemangkin 3 wt% and 5 wt% Ce-Ni/MgO yang baru menunjukkan bahawa pemangkin 5 wt% Ce-Ni/MgO mempunyai kawasan permukaan, isi padu liang dan diameter yang lebih besar daripada pemangkin 3 wt% Ce-Ni/MgO. Daripada pengimejan FESEM bagi pemangkin 5 wt% Ce-Ni/MgO, ia boleh diperhatikan bahawa pengagihan zarah logam di dalam pemangkin tersebut agak seragam. EDX bagi pemangkin 5 wt% Ce-Ni/MgO yang baru memaparkan bahawa hanya sedikit carbon didapati bagi pemangkin tersebut. Hal ini membuktikan bahawa pemangkin tersebut mempunyai kecekapan mengeluarkan karbon yang tinggi. Kajian tindak balas telah mendapati bahawa pemangkin 3 wt% and 5 wt% Ce-Ni/MgO memberikan kadar pembentukan hasil produk (H_2 and CO) yang hamper sama dan lebih tinggi daripada pemangkin Ni/MgO. Walaubagaimanapun, pemangkin 5 wt% Ce-Ni/MgO memberikan penukaran yang lebih tinggi sedikit berbanding dengan pemangkin 3 wt% Ce-Ni/MgO. Hal ini menunjukkan bahawa 5 wt% Ce-Ni/MgO merupakan pemangkin yang mempunyai prestasi yang tertinggi. Kemudian, ia dipilih untuk kajian tindak balas yang selanjutnya. Peningkatan suhu dalam tindak balas menyebabkan kadar pembentukan CO dan H_2 serta kadar penggunaan methane yang mematuhi prinsip Arrhenius. Penggunaan methane menunjukkan tenaga pengaktifan yang tertinggi, iaitu 62.59kJ/km

TABLE OF CONTENTS

SUPERVISOR'S DECLARATION	IV
STUDENT'S DECLARATION	V
<i>Dedication</i>	VI
ACKNOWLEDGEMENT	VII
ABSTRACT.....	VIII
ABSTRAK	IX
TABLE OF CONTENTS	X
LIST OF FIGURES	XII
LIST OF TABLES	XIV
LIST OF ABBREVIATIONS.....	V
LIST OF ABBREVIATIONS.....	XVI
1 INTRODUCTION	1
1.1 Background	1
1.2 Problem Statement	2
1.3 Objective	3
1.4 Scope of study	3
2 LITERATURE REVIEW	4
2.1 Introduction.....	4
2.2 Palm Oil Mill Effluent (POME).....	5
2.3 Dry Reforming of Methane	8
2.4 Steam Reforming of Methane	8
2.5 Partial Oxidation of Methane	9
2.6 Autothermal Reforming.....	10
2.7 Thermodynamics Analysis of Reactions in Biogas Dry Reforming.....	11
2.8 Reforming Catalyst.....	13
2.9 Catalyst Preparation Methods.....	18
2.10 Catalyst Deactivation.....	18
2.10.1 Sintering.....	19
2.10.2 Fouling.....	21
3 METHODOLOGY.....	26
3.1 Introduction.....	26
3.2 Materials Description.....	26
3.2.1 Catalysts.....	26
3.2.2 Gases.....	27
3.3 Catalyst Preparation.....	27
3.4 Catalyst Characterization.....	27
3.4.1 Brunauer- Emmett- Teller (BET).....	28
3.4.2 X-ray Photoelectron Spectroscopy (XPS).....	33
3.4.3 X-ray Diffraction (XRD).....	34
3.4.4 Field Emission Scanning Electron Microscopy - Energy Dispersive X-ray (FESEM-EDX).....	37

3.4.5	Thermogravimetric Analysis (TGA).....	38
3.4.5.1	Calcination.....	39
3.4.5.2	Non-isothermal Thermogravimetric Analysis.....	39
3.5	Catalyst Testing.....	40
4	RESULTS AND DISCUSSION	41
4.1	Fresh Catalyst Characterization	41
4.1.1	XRD Diffraction Pattern	42
4.1.2	Liquid N ₂ Physisorption.....	44
4.1.3	FESEM Imaging.....	44
4.1.4	EDX.....	45
4.1.5	Thermogravimetric Analysis (TGA).....	46
4.1.6	X-ray Photoelectron Spectroscopy (XPS).....	50
4.2	Dry Reforming Reaction Studies.....	56
4.2.1	Catalyst Screening.....	56
4.2.2	Effect of Reaction Temperature.....	58
4.3	Spent Catalyst Characterization.....	61
4.3.1	FESEM Imaging.....	61
5	CONCLUSIONS AND RECOMMENDATIONS	62
5.1	Conclusions	62
5.2	Recommendations	64
	REFERENCES	65
	APPENDICES	72

LIST OF FIGURES

Figure 2.1: Equilibrium constant of reactions involving in CH_4/CO_2 reaction at different temperatures at atmospheric pressure.....	12
Figure 2.2: Two conceptual models for crystallite growth due to sintering by (a) atomic migration and (b) crystallite migration.....	19
Figure 2.3: Normalized nickel surface area (based on H_2 adsorption) versus time during sintering of Ni/SiO_2 in hydrogen atmosphere.....	20
Figure 2.4: Illustration of pore closure at support due to sintering.....	20
Figure 2.5: Illustration of carbon depositions at catalyst support.....	22
Figure 2.6: Carbon formation on supported Ni-based catalyst.....	23
Figure 2.7: Carbon deposition as a function of temperature and CO_2/CH_4 ratio at 1 atm.....	24
Figure 3.1: Typical N_2 adsorption-desorption isotherms of mesoporous materials.....	30
Figure 3.2: Typical N_2 adsorption-desorption isotherms of large macroporous materials.....	30
Figure 3.3: Schematic diagram of a XPS apparatus.....	34
Figure 3.4: Schematic diagram of XRD (A) Collimation (B) Sample (C) Slit (D) Exit Beam Monochromator (E) Detector (X) Source of X-rays.....	36
Figure 3.5: Schematic diagram of FESEM.....	38
Figure 3.6: Schematic diagram of TGA.....	39
Figure 3.7: Experimental Setup of catalyst testing.....	40
Figure 4.1: XRD patterns for 5 wt% Ce-Ni/MgO catalyst.....	41
Figure 4.2: Isotherm plot for 3 wt% Ce-Ni/MgO.....	43
Figure 4.3: Isotherm plot for 5 wt% Ce-Ni/MgO.....	43
Figure 4.4: SEM image of 5 wt% Ce-Ni/MgO catalyst.....	44
Figure 4.5: EDX of 5 wt% Ce-Ni/MgO catalyst.....	45
Figure 4.6: Graph of derivative weight versus peak temperature for Ni/MgO catalyst at the heating ramp of $10^\circ\text{C}/\text{min}$	46

Figure 4.7: Graph of derivative weight versus peak temperature for 5wt% Ce-Ni/MgO catalyst for the heating ramp of 10°C/min.....	47
Figure 4.8: Graph of derivative weight versus peak temperature for 5wt% Ce-Ni/MgO catalyst for the heating ramp of 15°C/min.....	48
Figure 4.9: Graph of derivative weight versus peak temperature for 5wt% Ce-Ni/MgO catalyst for the heating ramp of 20°C/min.....	48
Figure 4.10: Kissinger model for two different catalysts.....	49
Figure 4.11: XP spectra of (a) Ni2p (b) Mg1s (c) O1s of fresh Ni/MgO catalyst.....	51
Figure 4.12: XP spectra of (a) Ni2p (b) Mg1s (c) O1s (d) Ce3d of fresh 3wt% Ce-Ni/MgO catalyst.....	53
Figure 4.13: XP spectra of (a) Ni2p (b) Mg1s (c) O1s (d) Ce3d of fresh 5wt% Ce-Ni/MgO catalyst.....	55
Figure 4.14: Rate of formation of both H ₂ and CO for Ni/MgO catalysts with different Ce loadings at 1123K and CH ₄ /CO ₂ ratio of 1:1.....	57
Figure 4.15: CH ₄ conversion with various cerium loadings at the first and second hour of the reaction.....	58
Figure 4.16: Variation of rate of formation of CO with temperature at CH ₄ /CO ₂ ratio = 1:1 at the first and second hour of the reaction.....	59
Figure 4.17: Variation of rate of formation of H ₂ with temperature at CH ₄ /CO ₂ ratio = 1:1 at the first and second hour of the reaction.....	59
Figure 4.18: Variation of rate of consumption of CH ₄ with temperature at CH ₄ /CO ₂ ratio = 1:1 at the first and second hour of the reaction.....	60
Figure 4.19: Plot of ln(r) versus 1/T for rate of formation of CO, H ₂ and rate of consumption of CH ₄	60
Figure 4.20: SEM image of spent 3 wt% Ce-Ni/MgO catalyst.....	61
Figure 4.21: SEM image of spent 5wt% Ce-Ni/MgO catalyst.....	61

LIST OF TABLES

Table 2.1: Characteristic of raw POME and the regulatory discharge limits.....	6
Table 2.2: Parameters limit for watercourse discharge of effluent from oil palm industry.....	6
Table 2.3: Reactions in CO ₂ reforming of CH ₄	11
Table 2.4: Summary of previous researches and their results.....	15
Table 2.5: Huttig temperatures, Tamman temperatures and melting points (K) of common compounds in heterogenous catalysis.....	21
Table 3.1 List of chemical and its purity.....	26
Table 3.2: List of gases and its purity.....	27
Table 4.1: Summary of values of 2-theta, intensity, inter plane distance of crystal (d-spacing) and crystallite size for the diffraction peaks.....	42
Table 4.2: BET specific surface area, pore volume and pore diameter of the catalyst samples.....	43
Table 4.3 Different heating ramps and maximum peak temperature for two uncalcined catalyst samples.....	49
Table 4.4: Activation energies of catalyst samples.....	50
Table 4.5: Binding energies of each element in fresh Ni/MgO catalyst and their corresponding count per unit second.....	51
Table 4.6: Binding energies of each element in fresh 3wt% Ce-Ni/MgO catalyst and their corresponding counts per unit second.....	53
Table 4.7: Binding energies of each element in fresh 5wt% Ce-Ni/MgO catalyst and their corresponding counts per unit second.....	56

LIST OF ABBREVIATIONS

P	gas pressure
P_s	saturation pressure of the adsorbate gas
V	volume of gas adsorbed
V_m	volume of gas adsorbed corresponding to monolayer coverage
c	a characteristic constant of the adsorbate
S_A	surface area of solid
a_m	average area occupied by a molecule
n_m	monolayer capacity of adsorbate
V_{liq}	volume of liquid N_2
V_{ads}	volume of nitrogen adsorbed
P_a	ambient pressure
r_k	Kelvin radius of the pore
γ	surface tension
E_k	kinetic energy
h	Planck's constant
ν	frequency
E_b	binding energy

Greek

ϕ	work function of spectrometer
λ	wavelength of X-ray beam
θ	angle of incidence
β_d	true line width at half maximum intensity
β_{ob}	observed width at half maximum intensity
β_{inst}	instrumental line width by standard

LIST OF ABBREVIATIONS

BET	Brunauer-Emmett-Teller
BOD	Biochemical oxygen demand
COD	Chemical oxygen demand
XRD	X-ray Diffraction
XPS	X-ray Photoelectron Spectroscopy
FESEM	Field Emission Scanning Electron Microscopy
EDX	Energy Disperse X-ray
POME	Palm oil mill effluent
POM	Partial oxidation of methane
TGA	Thermogravimetric analysis

CHAPTER 1 INTRODUCTION

1.1 Background

The excessive greenhouse gases (GHG) emission has led to climate change, consequently greenhouse gas utilizations has become an important area of research. In order to decrease the greenhouse gas emissions, numerous proposals stipulated under the Kyoto Protocol, (1997) had been implemented. One of the propositions is Clean Development Mechanisms (CDM) which aims at encouraging the cooperation between developing and developed countries in the activities of reduction in GHG emission (Yacob et al., 2005). The effects of GHG on climate change, sources and sinks of GHG, causes of GHG emissions and strategies of bridling GHG emission have been recently publicized (Bogner et al., 1995).

GHG especially carbon dioxide (CO₂) and methane (CH₄) are identified as main culprits that can cause global warming. In Malaysia, palm oil mill effluent (POME) anaerobic treatment widely-practiced in oil mills is a main source of CH₄ emission. Large amount of water is required in the palm oil extraction (Agamuthu, 1995) and therefore large volume of POME is created. On average, a palm oil mill will produce 0.65m³ POME for every ton of fresh fruit bunch (FFB) processed (Lim et al., 2013). A total of 32 million tons of POME was generated in 1990s (Ma, 1999) with average biochemical oxygen demand (BOD) reading of 25000 mg L⁻¹ and chemical oxygen demand (COD) of 50000 mg L⁻¹. When POME is anaerobically digested, biogas with 65% CH₄, 35% CO₂ and traces of H₂S would be produced (Yacob et al., 2005).

Significantly, CH₄ dry reforming can reduce environmental degradation since the reaction consumes CH₄ and CO₂ by converting the gases into synthesis gas (also known as syngas) and increases valorization of gas-field with high CO₂ content. Synthesis gas is a fuel gas mixture consists of CO, H₂ and very often than not, some CO₂. Synthesis gas

found applications in diverse areas i.e. as an intermediate in the production of synthetic natural gas (SNG), ammonia or methanol and a fuel of internal combustion engines. There are various methods to produce synthesis gas viz. steam reforming or dry reforming of natural gas or liquid hydrocarbons, the coal and biomass gasification, gasification of waste to energy etc. The catalytic CH₄-dry reforming can be carried out over various types of metallic catalysts. However, catalyst deactivation occurs easily in the reaction through carbon deposition on the catalyst surface. For example, Ni which is one of the best active metals is highly active and carbon layer forms easily on the Ni-based catalyst surface leading to deactivation of the catalyst. Zirconium-based mixed oxides are good supports for Ni-based catalyst in CH₄ dry reforming (Guczi et al., 2010). Cerium appears to be a very popular promoter for transition metal based catalysts in recent years since it is capable of storing large amount of oxygen (Daza et al, 2010).

1.2 Problem Statement

Palm oil production is a massive industry in Malaysia industry and its status as the main pillar of Malaysia's economy has been further endorsed via the Economic Transformation Program (ETP) mooted by PM Najib Tun Razak. One of the thrusts in ETP is the creation of biogas-capturing facilities targeted for every palm oil mill. Nonetheless, biogas as aforementioned is a potent greenhouse agent. Therefore, it provides the strongest motivation to the current work to utilize this biogas as the source of synthesis gas production.

Good catalytic performance of metallic catalyst is a very important criterion in the utilization of biogas to produce synthesis gas. The factors influencing the catalytic performance of supported metallic catalysts in biogas dry reforming are nature of metal, support type, conditions for catalyst preparation and pretreatment. By comparison in between nickel (Ni)-based catalyst and cobalt (Co)-based catalyst, Ni-based catalyst is more active yet cheaper than Co-based catalysts. Due to the highly active nature of Ni, Ni-based catalyst undergoes deactivation easily. Therefore, it is necessary to improve the

catalytic performance of Ni-based catalyst through the incorporation of suitable promoter into the catalyst. From literature, cerium (Ce) is a well-known promoter particularly for Ni-based catalyst. Therefore, it is worthy to explore the performance of Ce as a catalyst promoter for CH₄ dry reforming.

1.3 Objective

This research work aims to study the catalytic performance of Ce-Ni/MgO catalyst with various Ce loadings for CH₄ dry reforming.

1.4 Scopes of Study

In order to achieve the main objective of this work, the following scopes have been identified:

1. To prepare Ce-Ni/MgO with the 3% and 5% loadings of Ce via co-impregnation method.
2. To characterize the physicochemical properties of catalysts using methods such as:
 - i) Brunauer-Emmett-Teller (BET)
 - ii) X-ray Diffraction (XRD)
 - iii) X-ray Photoelectron Spectroscopy (XPS)
 - iv) Scanning Electron Microscopy- Energy Dispersive X-ray (SEM-EDX)
 - v) Thermo Gravimetric Analysis (TGA)
3. To study the catalytic activity and stability of the prepared catalysts with various Ce loadings in a bench-scale fixed-bed tubular reactor under different temperatures.

CHAPTER 2 LITERATURE REVIEW

2.1 Introduction

Palm oil industry is one of the leading agricultural industries in Malaysia with an average crude palm oil production of more than 13 million tons per year (H. Nour et al., 2011). Palm oil processing nonetheless produces POME which is a highly polluting wastewater. The disposal of POME into open ponds can potentially cause groundwater and soil pollution as well as the release of CH_4 into the atmosphere via natural organism degradation. According to Wu et al. (2010), enormous production of the crude palm oil has generated 44 million tons of POME in the year 2008 alone. On the average, for each ton of FFB processed, about 1 ton of liquid waste with BOD of 27 kg, COD of 62 kg, suspended solids (SS) of 35 kg and grease of 6 kg are produced (Saman., 2013).

Synthesis gas is not only an important feed for Fisher-Tropsch synthesis, but also a vital intermediate in several processes like gas-to-liquids and hydrogen production for refineries and fuel cells (Daza et al., 2010). Natural gas can be converted into synthesis gas through steam reforming, dry reforming and partial oxidation (Ross et al., 1996). Utilization of natural gas by CH_4 dry reforming has attracted much attention particularly industrial purposes. The H_2/CO ratio of 1 in CH_4 dry reforming leads to its application in Fisher-Tropsch synthesis (Rostrup-Nielsen et al., 2002).

In this chapter, the previous works related to biogas dry reforming and the combination of various active metals, supports and promoters will be critically discussed.

2.2 Palm Oil Mill Effluent (POME)

Palm oil is one of the world's most rapidly expanding equatorial crops. Indonesia and Malaysia are the two largest oil palm producers and were rich with numerous widespread, forest-dwelling species. According to Arif and Ariff (2001), oil palm currently occupies the largest area of farmed land in Malaysia. The total oil palm acreage increases from 320 to 3338 hectares from 1970 to 2000.

The processing of fresh fruit bunches (FFB) of oil palm can generate different types of waste substances. Among the waste substances generated, palm oil mill effluent (POME) is considered the most harmful waste for the environment and thus needs to be discharged with proper treatment. Fresh POME is a hot, acidic (pH between 4 and 5), brownish colloidal suspension containing high concentrations of organic matter, high amounts of total solids (40500 mg/L), oil and grease (4000mg/L), COD (50000 mg/L) and BOD (25000 mg/L) (Ma, 2000). The quality of the raw material and palm oil production processes in palm oil mills are the dependent variables of the characteristics of POME. The characteristics of typical POME are given in Table 2.1. Huge amount of water is required in the crude palm oil (CPO) extraction from FFB. For 1 ton of CPO, approximately 5-7.5 ton of water is required and more than 50% of water ends up as POME (Ma, 1999). Sterilization of FFB, clarification of the extracted CPO and hydro-cyclone separation of cracked mixture of kernel and shell hydrocyclone are the processing operations responsible for production of POME in the mills (Sethupathi, 2004). Sterilization contributes to 36% of POME production, clarification of the extracted CPO contributes to 60% of POME production and hydrocyclone separation of cracked mixture of kernel and shell hydrocyclone contributes to 4% of POME production (Sethupathi, 2004).

Table 2.1 Characteristics of raw POME and the regulatory discharge limits (Ma, 2000)

Parameters	Value*
Temperature	353-363
pH	4.7
Biochemical Oxygen Demand BOD ₃ ; 3 days at 303K	25000
Chemical Oxygen Demand (COD)	50000
Total Solids (T.S.)	40500
Total Suspended Solids (T.S.S)	18000
Total Volatile Solids (T.V.S)	34000
Oil and Grease (O&G)	4000
Ammonia-Nitrate (NH ₃ -N)	35
Total Kjeldahl nitrogen (TKN)	750

*All values, except pH and temperature, are expressed in mg/L

POME contains considerable amounts of N, P, K Mg and Ca (Habib et al., 1997) which are essential for plant growth. Table 2.2 lists the parameter limits for POME watercourse discharge from oil palm industry.

Table 2.2: Parameters limits for watercourse discharge of effluent from oil palm industry (Pierzynski, 2005)

Parameter	Units	Parameter limits for POME discharge	Remarks
Biochemical oxygen demand (BOD, 3-day, 303K)	mg/L	100	-
Chemical oxygen demand (COD)	mg/L	*	-

Total solids	mg/L	*	-
Suspended solids	mg/L	400	-
Oil and grease	mg/L	50	-
Ammoniacal nitrogen	mg/L	150	Value of filtered sample (GF/B)
Total nitrogen	mg/L	200	Value of filtered sample (GF/B)
pH	-	5-9	-
Temperature	K	318	-

Note: *No discharge standard after 1984

POME is considered as non-toxic since there are no uses of chemical additives during the oil extraction process. However, aquatic pollution can be caused by discharging of POME into water through the reduced level of dissolved oxygen content in water (Khalid and Wan Mustafa, 1992). Other than aquatic pollution, POME can cause greenhouse gas (GHG) emissions (Yacob et al., 2005). POME anaerobic treatment emits biogas mixture which contains a significant amount of CH₄ and CO₂ released from POME which is a major source of greenhouse emission. An approximately 9 kg CH₄/ton FFB is released from POME (at 0.7 m³ POME/ton FFB, 28 m³ biogas/m³ POME and 65% CH₄ in the biogas) (Wijbrans and Van Zutphen, 2005). Various treatment pathways have been tested to improve POME treatment and to reduce CH₄ emissions in order to solve the environmental problem. The technologies include biogas capturing technologies which involve the flaring of biogas or conversion of biogas to electricity or heat which convert methane to biogenic CO₂. The biogas capturing technologies can help to reduce GHG emissions with a factor of 23 (Klaarenbeeksel, 2009).

2.3 Dry Reforming of Methane

The dry reforming process is more industrially advantageous than steam reforming or partial oxidation in syngas production since H₂:CO product ratio is close to unity and thus it is suitable for further use in the production of oxygenated compounds and liquid hydrocarbons (He et al., 2009). The methane dry reforming can be represented by the following equation:

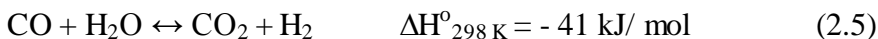


CH₄ dry reforming is highly endothermic as shown in Equation (2.1). Therefore, high temperatures are required in order to achieve high conversions of CH₄ and CO₂. However, catalyst will become deactivated easily at high temperature due to coke deposition (Ballarini et al., 2005) and/or sintering of the metallic phase and support (Guo et al., 2004). Coke deposition comes from CH₄ decomposition (cf. Equation (2.2)) and CO disproportionation (cf. Equation (2.3)). The CH₄ decomposition is endothermic and hence favoured at higher temperature and pressure. In contrast, CO disproportionation is exothermic and favoured at lower temperature and higher pressure. According to Tsyganok et al. (2004), a partial oxidation of CH₄ which is slightly exothermic may be combined with a highly endothermic CH₄ dry reforming.



2.4 Steam Reforming of Methane

CH₄ steam reforming is an equilibrium-limited process and consists of several reversible reactions.



The Equations (2.4) and (2.6) show highly endothermic CH₄ steam reforming reactions whereas Equation (2.5) shows the moderately exothermic water-gas-shift (WGS) reaction. Equation (2.6) is the combination of Equations (2.4) and (2.5). High temperature is required for the endothermic behavior of reactions in Equations (2.4) and (2.6). From the Equations (2.4) and (2.6), the increase of the total gas volume in the reactions causes low pressure to be favoured in the CH₄ steam reforming. WGS is slightly exothermic and therefore favoured at low temperature. Pressure change has negligible effect on the reaction since there is no change in total gas volume in the reaction. CH₄ steam reforming and WGS reactions are typically carried out over a supported Ni catalyst at high temperatures, typically above 773 K (James, 2006).

Highly pure gaseous hydrogen can be obtained in CH₄ steam reforming since the product of the reaction has the highest H₂/CO ratio. The requirement of high temperature in CH₄ steam reforming leads to expensive operation cost for the reaction. In order to save the operation cost, the reaction may be replaced with auto thermal reforming and partial oxidation which are more economic viable (Armor, 1999).

2.5 Partial Oxidation of Methane

Partial oxidation of CH₄ is a combination of steam reforming, dry reforming and combustion of CH₄ (Chen et al., 2012). There are two types of partial oxidation of CH₄, namely catalytic partial oxidation and non-catalytic partial oxidation of CH₄. For catalytic partial oxidation of CH₄, CH₄ reacts with O₂ in the presence of catalyst to produce synthesis gas with H₂/CO ratio of approximately two (Maxim et al., 2004). For non-catalytic partial oxidation of CH₄, CH₄ reacts with O₂ to produce synthesis gas at high temperatures of 1200 to 1500 °C in the absence of catalyst (James, 2006). Hickman and Schmidt (1992) revealed that complete conversion of CH₄ to H₂ and carbon in partial oxidation occurs at reaction times as short as 1.0 ms. Therefore, partial oxidation of CH₄ requires smaller reactor size and is less complex as compared to other synthesis gas production technologies.

The scheme of the partial oxidation of CH₄ is shown as:



The exothermic behavior of CH₄ partial oxidation causes lower amount of thermal energy to be required in the reaction and thus more economical than steam reforming and dry reforming (Peña et al., 1996). However, requirement of pure oxygen flow causes it to be an expensive process (Peña et al., 1996). It is risky due to the possibility of explosion caused by CH₄ and O₂ if the reaction is not conducted carefully (Peña et al., 1996).

Partial oxidation is very important to produce H₂ and it is characterized by auto thermal reaction. Excess enthalpy recovery, gas hourly space velocity (GHSV), number of turns and atomic O:C ratios affect the efficiency of partial oxidation in terms of H₂ yield (Chen et al., 2012). The H₂ yield from partial oxidation can be enhanced by preheating reactants through waste heat recovery, increasing GHSV and increasing number of turns. Maximum hydrogen yield can be achieved at O:C ratio of 1.2 (Chen et al., 2012).

2.6 Autothermal Reforming of Methane

The auto thermal reforming of CH₄ is a combination of steam reforming and partial oxidation of CH₄. Hence, it involves CH₄, H₂O and O₂ in the presence of catalyst. The name “auto thermal” came from its property that consumes the thermal energy generated by itself (Ayabe et al., 2003). The thermal energy is generated in the partial oxidation of CH₄ and this property makes it to be energy saving (Ayabe et al., 2003). Similar as other reforming processes of CH₄, auto thermal reforming is also used to produce synthesis gas. The fractions of gaseous reactant can affect the H₂:CO ratio in the synthesis gas produced in auto thermal reforming (Palm, 2002). The typical range of H₂/CO ratio in the product is 1 to 2 (Palm, 2002).

2.7 Thermodynamics Analysis of Reactions in Methane Dry Reforming

Table 2.3 shows the main reactions which may occur in CH₄ dry reforming.

Table 2.3 Reactions in CH₄ dry reforming (Nikoo and Amin, 2011)

Reaction number	Reaction	ΔH_{298K} (kJ/mol)
1	$\text{CH}_4 + \text{CO}_2 \leftrightarrow 2\text{CO} + 2\text{H}_2\text{O}$	247
2	$\text{CO}_2 + \text{H}_2 \leftrightarrow \text{CO} + \text{H}_2\text{O}$	41
3	$2\text{CH}_4 + \text{CO}_2 \leftrightarrow \text{C}_2\text{H}_6 + \text{CO} + \text{H}_2\text{O}$	106
4	$2\text{CH}_4 + 2\text{CO}_2 \leftrightarrow \text{C}_2\text{H}_4 + 2\text{CO} + 2\text{H}_2\text{O}$	284
5	$\text{C}_2\text{H}_6 \leftrightarrow \text{C}_2\text{H}_4 + \text{H}_2$	136
6	$\text{CO} + 2\text{H}_2 \leftrightarrow \text{CH}_3\text{OH}$	-90.6
7	$\text{CO}_2 + 3\text{H}_2 \leftrightarrow \text{CH}_3\text{OH} + \text{H}_2\text{O}$	-49.1
8	$\text{CH}_4 \leftrightarrow \text{C} + 2\text{H}_2$	74.9
9	$2\text{CO} \leftrightarrow \text{C} + \text{CO}_2$	-172.4
10	$\text{CO}_2 + 2\text{H}_2 \leftrightarrow \text{C} + 2\text{H}_2\text{O}$	-90
11	$\text{H}_2 + \text{CO} \leftrightarrow \text{H}_2\text{O} + \text{C}$	-131.3
12	$\text{CH}_3\text{OCH}_3 + \text{CO}_2 \leftrightarrow 2\text{CO} + 4\text{H}_2$	258.4
13	$3\text{H}_2\text{O} + \text{CH}_3\text{OCH}_3 \leftrightarrow 2\text{CO}_2 + 6\text{H}_2$	136
14	$\text{CH}_3\text{OCH}_3 + \text{H}_2\text{O} \leftrightarrow 2\text{CO} + 4\text{H}_2$	204.8
15	$2\text{CH}_3\text{OH} \leftrightarrow \text{CH}_3\text{OCH}_3 + \text{H}_2\text{O}$	-37
16	$\text{CO}_2 + 4\text{H}_2 \leftrightarrow \text{CH}_4 + 2\text{H}_2\text{O}$	-165
17	$\text{CO} + 3\text{H}_2 \leftrightarrow \text{CH}_4 + \text{H}_2\text{O}$	-206.2

Figure 2.1 shows the equilibrium constant of reactions involved in CH₄ dry reforming at different temperatures and atmospheric pressure.

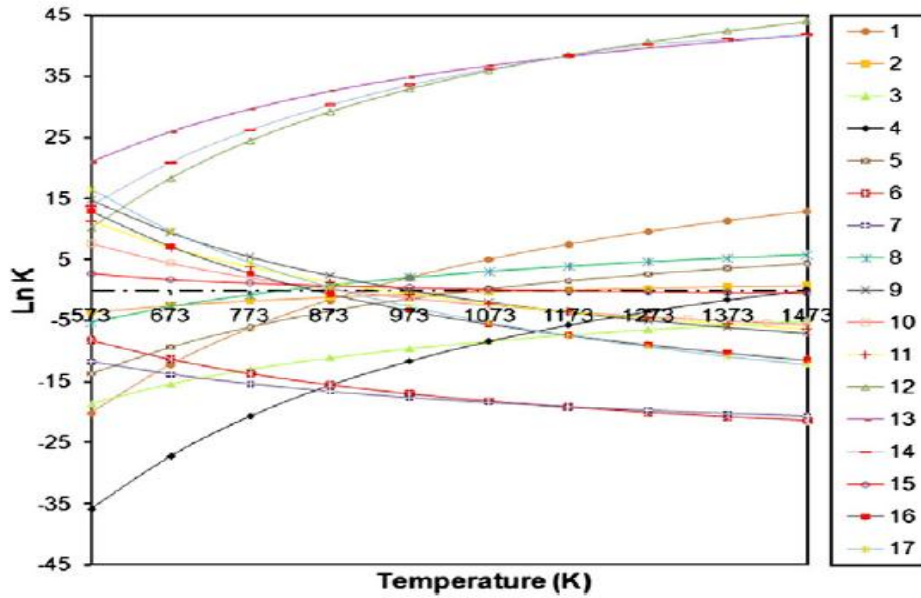


Figure 2.1 Equilibrium constant of reactions involved in CH₄ dry reforming at different temperatures and atmospheric pressure (Nikoo and Amin, 2011)

According to thermodynamic principles (Smith, 2005), negative value of Gibbs free energy change of reaction (ΔG_t) is an indication of spontaneous reaction whereas positive value of ΔG_t is an indication of thermodynamically limited reaction. Equilibrium constant (K) determines to which the extent of the reaction occurs. Reactions having the value of K higher than unity cannot be shifted to the opposite side by changing the molar ratio of the reactants whereas reactions having the value of K close to unity will have significant change in product distribution when the molar ratio of the reactants are varied (Wang et al., 2009). For those reaction with negative value of ΔG_t , larger $\ln(K)$ indicates greater feasibility of the reactions.

From Figure 2.1, CH₄ dry reforming (reaction 1) is favorable at temperature higher than 1000K in agreement with the temperature range suggested in the previous study (Istadi, 2005). Reverse water gas-shift (RWGS) reaction (reaction 2) is much influenced by equilibrium within the entire investigated temperature range. Generally, CH₄ dry reforming and RWGS reaction occur simultaneously. The CO₂ oxidative coupling of CH₄ reactions (reactions 3 and 4) possess high negative values of $\ln(K)$ at low temperatures showing that the reactions are not feasible at low temperature.

Although ethane (C_2H_6) dehydrogenation (reaction 5) can be influenced by equilibrium limitations, it still can occur at higher temperature to produce ethylene (C_2H_4). Reaction 5 usually takes place along with reactions 3 and 4 (Istadi, 2005). Negative values of $\ln(K)$ for hydrogenation of CO_2 and CO (reactions 6 and 7) show that the reverse reactions are more favorable than the forward reactions particularly at high temperature.

CH_4 decomposition (reaction 8), CO disproportionation (reaction 9), CO_2 hydrogenation (reaction 10) and CO hydrogenation (reaction 11) may form carbon even though changing molar ratio of reactants affects the reactions due to their low value of $\ln(K)$. Reaction 8 has the higher tendency to form carbon at higher temperature whereas reactions 9, 10 and 11 has higher tendency to produce carbon at lower temperature ($< 800K$) and can be influenced by equilibrium limitations at higher temperature. The tendency of the forward reactions in reactions 12, 13 and 14 within the whole temperature range considered can be improved whereas reaction 15 is easily influenced by equilibrium limitations. The positive values of $\ln(K)$ at low temperature for methanation (reactions 16 and 17) indicate that they are more feasible at low temperatures. They are less feasible at high temperature due to negative $\ln(K)$ and exothermic behavior.

2.8 Reforming Catalyst

There are various types of active metals such as Ni, Co, Fe (Araujo, 2008) and noble metals such as Pt, Rh, Pd, Ir (Erdohelyi, 1994) for catalysts in CH_4 dry reforming. Ni-based catalyst is one of the best reforming catalysts. However, Ni metal is very reactive and therefore carbon layer forms easily on the catalyst which can cause deactivation of the catalyst (Guczi et al., 2010). Therefore, several techniques have been used to modify the Ni metal by using various supports or adding second metal to Ni metal (Guczi et al., 2010). Although Ni-based catalysts become deactivated easily, there are still usually employed in CH_4 dry reforming because Ni metal is cheap and easily available (Xu et al., 2001). In CH_4 dry reforming, Ni and Fe elements are more reactive than Cu, Fe and Co for TiO_2 supported catalysts (Bradford & Vanice, 1999). The activity of the catalysts

containing Fe, Co, or Cu is almost the same as that of the supported catalyst with no active metal and much lower than that of the catalyst containing Ni irrespective of the support used (Bradford & Vanice, 1999).

Support can influence both catalytic activity and stability considerably (Nagaoka, 2001). Supports which are able to provide oxygen to metal during reaction can help to reduce carbon deposition (Wang, 2000). Therefore, metallic oxides having high oxygen exchange capacity and mobility are good choice of supports for CH₄ dry reforming. There are various metallic oxides used as support on which the active metals are usually dispersed like Al₂O₃, MgAl₂O₄, CeO₂, ZrO₂ and so on. ZrO₂ is better than Al₂O₃ or SiO₂ which are unable to be reduced in terms of its redox behavior, surface acidity, reducibility and thermal stability (Bradford, 1998). Spc-Ni/Mg-Al catalyst prepared from hydrotalcite-like precursor has a higher activity than those prepared by conventional impregnation method such as Ni/g-Al₂O₃ and Ni/MgO (Shishido et al., 2001).

Addition of promoter into a catalyst helps to increase the reducibility of metal on the support and create more active site for the catalyst, thus improving the performance of the catalyst. Promoter can be an alkali earth metal, noble metal or rare earth metal. Rare earth metal oxide like CeO₂ is a good promoter to noble metal catalyst as it helps to increase the catalytic reactivity in the oxidation reactions of hydrocarbons (Alvarez-Galvan et al., 2008) and enhance the performance characteristics of three-way catalysts used in removal of pollutants in automobile exhaust (Farrauto et al., 1999). CeO₂ has high basicity and high reducibility, so active metals can be well dispersed on the support and thus improving the oxidation and reduction cycle of noble metals (Damyanova, 2003). In addition, the high oxygen storage capacity of reduced CeO₂ can help to remove carbon deposited from the catalyst surface (Damyanova, 2003). Table 2.4 shows the summary of previous researches about reforming catalyst and their results.

Table 2.4 Summary of previous researches about reforming catalysts and their results

Catalyst	Results	Reference
Incorporation of Co as promoter to Ni/MgO-ZrO ₂ catalyst	-Co stabilized t-phase in ZrO ₂ , gave better metal dispersion and reduced metal particle size.	(Fan et al., 2010)
Addition of Cu as promoter to Ni-based catalyst	-Cu stabilized the structure of active sites on Ni surface for CH ₄ cracking reaction. -Stabilization of the active sites prevented metal sintering or loss of nickel crystallites.	(Chen et al., 2004)
Zr-Ni-MCM-41 catalyst	-Zr improved activity and long-term stability of catalyst significantly. -Zr enhanced the structural stability and dispersion of active sites of Ni.	(Liu et al., 2009)
K and Li promoted Ni/Al ₂ O ₃ and Ni/CeO ₂ catalysts	-Addition of K and Li reduced carbon deposition but decreased reactant conversions and H ₂ /CO ratio of the products.	(Barroso-Quiroga et al., 2010)
Incorporation of Ca to Ni/Al ₂ O ₃ catalyst	-Addition of Ca decreased catalytic activity dramatically and increased carbon deposition greatly. -Interaction of Ca with Al ₂ O ₃ increased the extent of metal sintering.	(Luna et al., 2008)
Ni-Mg/HY catalyst	-Addition of Mg reduced the size of Ni particles, produced highly dispersed Ni particles and slowed down the sintering of Ni	(Jeong et al., 2006)

	particles on the catalyst surface.	
Promotion of Ni/Al ₂ O ₃ with La ₂ O ₃ and CeO ₂	-La ₂ O ₃ and CeO ₂ suppressed the sintering of Ni particles and delayed the transition of the Al ₂ O ₃ support from γ -Al ₂ O ₃ to α -Al ₂ O ₃ .	(Yang et al., 2010)
	-La ₂ O ₃ and CeO ₂ induced formation of reactive filamentous carbon on the catalyst and increased the amount of CO ₂ adsorbed on the catalyst surface.	(Zhang et al., 2005)
	-La ₂ O ₃ and CeO ₂ increased reducibility of the catalyst and enhanced the degree of dispersion of Ni particles.	(Junke et al., 2009)
Incorporation of Yb (1 wt%-8wt%) into Ni/ γ -Al ₂ O ₃ catalysts	-Addition of 1-2 wt% Yb increased the catalytic activity and stability significantly and produced H ₂ and CO in ratio of 0.95.	(Amin et al., 2012)
	-Addition of 3-8 wt% Yb did not increase the activity significantly.	
	-Addition of 2 wt% Yb produced catalyst with smallest average Ni particle size, narrowest particle size distribution, fewest carbon deposited, highest reducibility and high degree of graphitized carbon.	
Incorporation of vanadium into MCM-41 type mesoporous materials by a one-pot synthesis route	-A highly active, selective and stable catalyst was generated for selective oxidation reactions.	(Gucbilmez et al., 2006)

Addition of Pt to Ni ₃ Al intermetallide	<p>-Addition of low amount of Pt reduced carbon deposition and increase long term stability.</p> <p>-Pt prevented Ni metal sintering by avoiding particle coalescence.</p>	(Larisa et al., 2011)
α -Al ₂ O ₃ and γ -Al ₂ O ₃ supported catalyst	<p>-α-Al₂O₃ supported catalyst had high chemical, physical stability and mechanical resistance.</p>	(Marturano et al., 1997)
	<p>-α-Al₂O₃ supported catalyst had low specific surface area and metal particles sintering occurs easily.</p>	(Christensen et al, 2006)
	<p>-γ-Al₂O₃ supported catalyst had a larger specific surface area and the metal particles are highly dispersed and stable.</p>	(Albertazzi et al., 2003)
	<p>-γ- Al₂O₃ was acidic support and can cause carbon formation and metal sintering easily leading to catalyst deactivation.</p>	
Bimetallic phosphorus-promoted PdNi/ Al ₂ O ₃ catalyst (1 wt% phosphorus, 3 wt % phosphorus and 5 wt% phosphorus)	<p>-For 1 wt% phosphorus-loaded PdNi/Al₂O₃ catalyst, well NiO particles and NiAl₂O₃ spinel structure were formed.</p>	(Damyanova et al., 2011)
	<p>-For 3 wt% and 5 wt% phosphorus-loaded PdNi /Al₂O₃ catalysts, NiO particles were bigger.</p>	

Ru/La₂O₃-SiO₂ catalysts (15 wt%, 27 wt%, 40wt% and 50 wt% of La₂O₃ supports) -Ru/La₂O₃ (50) – SiO₂ had the highest forward turn over frequency with 38% dispersed Ru. (Faroldi et al., 2011)

2.9 Catalyst Preparation Methods

Several preparation methods can be used to develop catalyst for CH₄ dry reforming. Physical characteristics of the catalyst can be influenced by the preparation method used (Neiva et al., 2007). Thus, preparation method should be chosen based on the best physical characteristics of the material used for obtaining the expected catalyst.

Impregnation of metal salt in aqueous solution onto a support material such as Al₂O₃ is the most common catalyst preparation method. Other than that, co-precipitation method is also usually applied in catalyst preparation. For co-precipitation method, solutions of metal salts are usually mixed together at constant pH and then precipitated into the desired product. After that, the catalyst prepared will be allowed for calcination and/ or reduction. Calcination means heating of catalyst sample in air in order to remove the carbon deposited on the catalyst surface whereas reduction refers to heating of the catalyst sample in reducing atmosphere containing hydrogen for catalyst metal activation (Wang & Lu, 1998).

2.10 Catalyst Deactivation

Catalyst is widely used in many industrial processes in order to decrease the activation energy of a chemical reaction and therefore speed up the reaction. Catalyst deactivation is a major issue of CH₄ dry reforming. Catalyst deactivation often lead to poorer product yield, additional energy consumption and production time loss associated with catalyst replacement, regeneration and plant shut-down costing industries billions of dollars annually (Bartholomew, 2001). Although deactivation is unavoidable in the operation of catalytic reactors, it is possible to delay the process and to minimize its effects, for example, the formulation of deactivation-resistant catalysts, the optimal operation of catalytic reactors that suppress deactivation or the execution of specific reactivating

procedures (Forzatti and Lietti, 1999). Catalyst deactivation is commonly caused by sintering and coking. The mechanisms of sintering and fouling (coking) are discussed briefly in this section.

2.10.1 Sintering

Sintering or aging in catalysis means the loss of active surface area due to structural modification. According to Mouljin et al. (2001), sintering occurs in all stages in the life cycle of a catalyst from preparation (local heating during calcination), reduction, reaction (hot spots, maldistribution) to regeneration (coke burn-off). In supported metal catalysts, smaller surface area may be the consequence of growth of metallic crystallites (as implicated by decreasing surface-to-volume ratios). In theory, sintering takes place through atomic migration and crystallites migration as shown in Figure 2.2.

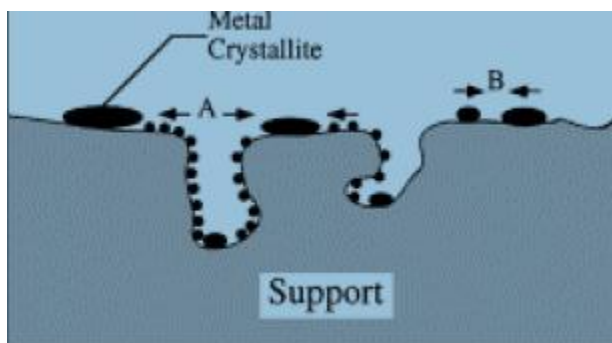


Figure 2.2 Two conceptual models for crystallite growth due to sintering by: (a) atomic migration; and (b) crystallite migration (Bartholomew, 2001)

In atomic migration, active atoms are separated from the crystallites where they migrate along the support surface and then captured by larger crystallites. In crystallite migration, a crystallite migrates across the support surface followed by collision and coalescence (Bartholomew, 2001).

Sintering is mostly caused by prolonged exposure of catalyst to high temperature. Figure 2.3 shows the effect of temperature on the extent of sintering in Ni-based catalysts as a function of time. The loss of normalized surface area (defined as the ratio of nickel surface area at instantaneous time to its initial surface area) increased with the increasing

temperature usage. From Figure 2.3, the nickel surface areas decreased quickly in the first 15 h, then remained almost constant up to 50 h.

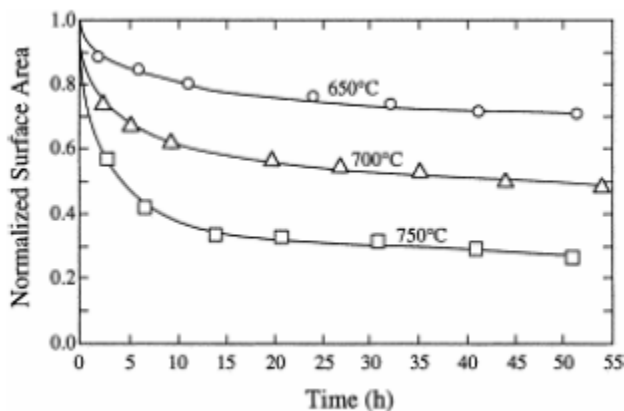


Figure 2.3 Normalized nickel surface area (based on H₂ adsorption) versus time during sintering of Ni/SiO₂ in hydrogen atmosphere (Bartholomew, 2001)

Porous catalyst supports also undergo consequences of thermally-induced sintering. Pores on the catalyst supports will become narrow and ultimately closed as a result of the flow of solid support material. Thus, no substance can enter into the catalyst interior and surface area is lost. Figure 2.4 shows the phenomenon of pore closure due to sintering.

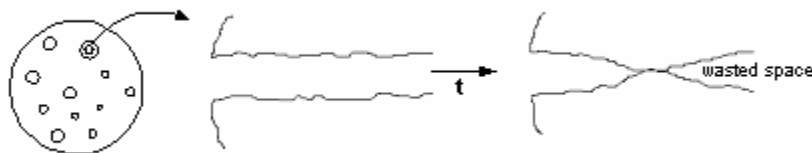


Figure 2.4 Illustration of pore closure at support due to sintering (Fogler, 1999)

Choosing temperature ranges carefully can help to slow down the sintering of metal and support effectively. The temperature range recommended is 0.3-0.5 times the melting point of metal and support (Moulijin et al., 2001). The temperature of 0.3 times melting point is known as Huttig temperature. At this temperature, atoms at defects gain mobility. The temperature of 0.5 times melting point is known as Tamman temperature. At this temperature, atoms from the bulk become mobile. Table 2.5 lists the Huttig temperatures,

Tamman temperatures and melting points of some common compounds in heterogeneous catalysis.

Table 2.5 Huttig temperatures, Tamman temperatures and melting points (K) of common compounds in heterogeneous catalysis (Moulijin et al., 2001)

Compound	T _{Huttig}	T _{Tamman}	T _{melting}
Pt	608	1014	2028
PtO	247	412	823
Pd	548	914	1828
PdO	307	512	1023
Rh	677	1129	2258
Ru	817	1362	2723
Fe	542	904	1808
Co	526	877	1753
Ni	518	863	1725
NiO	669	1114	2228
Ag	370	617	1233

Strengthening metal-support interactions can help to enhance catalyst resistance towards sintering. Other than that, introduction of promoters such as BaO, CeO₂, La₂O₃, SiO₂ and ZrO₂ will lead to increased support stability by preventing surface restructuring of alumina-supported metal catalysts (Burtin et al., 1987). Thus, sintering can be minimized by introducing suitable promoters.

2.10.2 Fouling

Fouling is the phenomenon in which active surface area is covered by a deposit of species that comes from the fluid phase. Combustion ashes, wear residues from process equipment, asphaltenes during processing of heavy petroleum fractions and carbonaceous residues from dehydrogenation in hydrocarbon processing are some of the substances that

may cause deposition (Moulijin et al., 2001). Carbon deposition is the major issue in CH₄ dry reforming and it hinders reactants from entering onto the catalyst used. At reactor level, interparticle coke growth causes excessive pressure drop across the reactor and finally termination of fluid flow leading to shut-down of the reactor operation. The happening of carbon deposition over the surface of supported metal catalyst is shown in Figure 2.5.

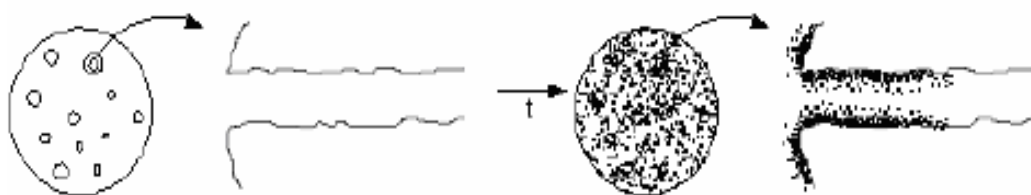


Figure 2.5 Illustration of carbon depositions at catalyst support (Fogler, 1999)

The effect of coke on the activity of reforming catalyst depends on both quantity of coke and the location of coke deposition. The extent of pore blockage caused by the coke deposited on pore mouths is greater than that distributed on the inner wall of the support if the same amount of coke is deposited in both areas (Richardson, 1972).

CO disproportionation produces elemental carbon which can further polymerize to form amorphous and graphitic carbon, metal carbide or dissolve into the bulk of the metal to create whisker-like or vermicular carbon (Bell, 1987). The graphitic carbon is highly stable and can be transformed from amorphous carbon at high temperatures (> 773 K) over a period of time. The hydrocarbon cracking produces various partially hydrogenated species, i.e. CH_x and C_nH₂ which condense to form high molecular weight coke on the catalyst surface (Bartholomew, 2001). Figure 2.6 shows the growth of carbon filaments on a supported Ni-based catalyst.

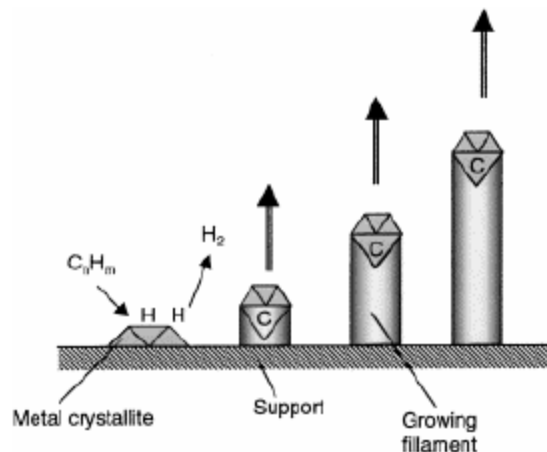


Figure 2.6 Carbon formation on supported Ni-based catalyst (Moulijn et al., 2001)

Initially, hydrocarbon molecules are adsorbed on the active particle surface releasing gaseous products and atomic carbons. Even though the surface carbon can be gasified easily, carbon eventually diffuses in the form of Ni carbide intermediate through the Ni crystallite to the rear side (Renshaw et al., 1971). As carbon reaches the support, whisker nucleation occurs where the growth of filamentous carbon starts as more carbons diffuse. Nickel particle will be separated from the support as result of the filament elongation and sits on the ‘head’ of the carbon whiskers rooted in the support (Bell, 1987). During the filament elongation, the catalyst will remain active until sufficient pyrolytic carbon encapsulates the Ni particles preventing further adsorption (Bell, 1987). The formation of filamentous carbon on a supported metal catalyst at a given reaction condition depends on metal type, crystallite size and support characteristic.

There are several ways of alleviating the problem of carbon deposition in dry reforming reaction. Firstly, increasing the CO_2/CH_4 ratio in the feed (> 1) can help to avoid carbon deposition (Guczi et al., 2010). It is due to the fact that when CH_4 becomes more intensively a limiting reactant, the extent of carbon formation in CH_4 cracking will be smaller. Figure 2.7 shows the carbon deposition as a function of temperature and CO_2/CH_4 ratio at 1 atm.

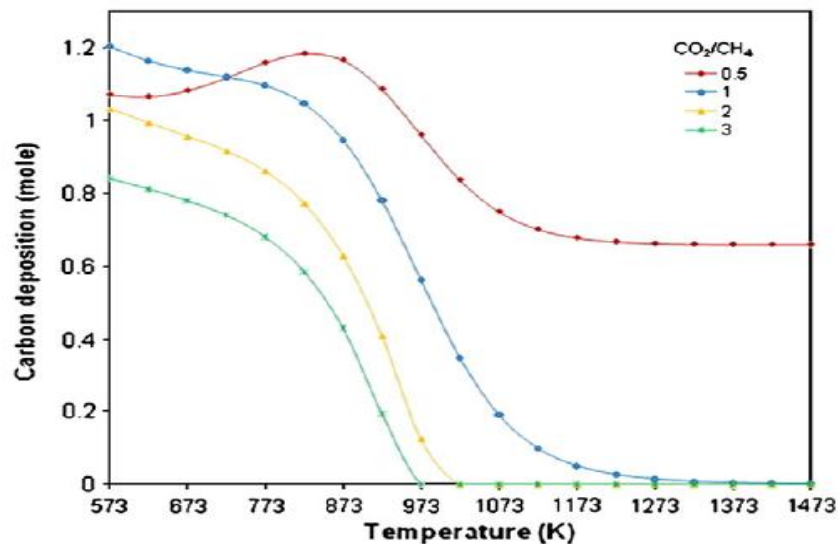


Figure 2.7 Carbon deposition as a function of temperature and CO₂/CH₄ ratio at 1 atm

Carbon deposited on the metallic catalyst during CH₄ dry reforming can also be removed by the addition of O₂ and steam. The activity of catalyst deactivated by carbon deposition can be restored when O₂ and steam are passed over Ni-based catalyst in CH₄ dry reforming (Zhang et al., 1998). According to Aiello et al. (2000), Ni/SiO₂ could be fully regenerated at 650°C with steam for up to 10 successive cracking/ regeneration cycles without substantial loss of activity of the catalyst. Among O₂, CO₂ and steam, oxidation of catalyst with O₂ can remove carbon most efficiently (Zhang et al., 1998).

Other than that, addition of promoter in small quantity to metallic catalyst can help to reduce the carbon deposition on the catalyst surface. According to Choudhary et al.(1998), addition of small amount of sulphur can help to block the sites of carbon formation and thus reduce the amount of carbon deposited on the catalyst. Addition of alkali and rare earth oxides in small quantity can also prevent carbon formation problem effectively (Horiuchi et al., 1996). Use of Ce-promoted catalysts with the presence of transition metals has been practiced widely in recent years due to their high oxygen storage capability. Lattice O₂ in CeO₂ is eliminated during reduction and creation of anionic vacancies (CeO_{2-x}) gives high lattice O₂ mobility and offers reactive sites on the surface of metal oxides. As a result, the carbon on the catalyst surface will tend to react with O₂

to produce CO₂ more frequently and thus less carbon are deposited on the catalyst surface (Daza et al., 2010).

In addition, carbon deposition can be reduced through the use of bimetallic catalyst. The roles of the second metal in bimetallic catalysts in overcoming the problem of carbon deposition include modification of electronic properties of active metal particles (Burch and Garla, 1981), dilution of active metal surface into smaller entities (Coq and Figueras, 1984), providing sites for hydrogenation of carbon deposits (Parera and Beltramini, 1988) and decreasing the solubility of carbon within the metal lattice (Bartholomew, 1980). It was reported that rhenium (Re) (Klulsdahl, 1968), iridium (Ir) (Sinfelt, 1979), tin (Sn) (Muller, 1979), germanium (Ge) (Bouwman and Biloen, 1977) and gold (Au) (Biloen et al., 1977) have been added to Pt/Al₂O₃ catalysts. All these bimetallic catalysts were reported to have enhanced catalytic properties in terms of activity and stability compared to the monometallic Pt catalyst. According to Guzi et al.(2010), addition of 0.5 wt% Au to Ni/MgAl₂O₄ improved the catalytic activity by reducing the formation of carbon multi-walled nanotubes and increasing the degree of dispersion of Ni metals on the catalyst.

Chapter 3 METHODOLOGY

3.1 Introduction

This section covers materials description, catalysts preparation, catalyst characterization and catalyst test. The characterization techniques involve Brunauer- Emmett-Teller (BET), X-ray photoelectron spectroscopy (XPS), X-ray diffraction (XRD) and Field Emission Scanning Electron Microscopy-Energy Dispersive X-ray (FESEM-EDX). Furthermore, the theoretical fundamentals and operational procedures of catalyst characterization instruments will also be discussed.

3.2 Materials Description

3.2.1 Catalysts

The catalyst employed in the current work is Ce-promoted Ni/MgO catalyst. All the materials required for preparing this catalyst such as cerium nitrate, nickel nitrate and magnesium oxide are supplied by Sigma-Aldrich Sdn. Bhd. (cf. Table 3.1).

Table 3.1 List of chemical and its purity

Chemical	Purity
Cerium nitrate ($\text{Ce}(\text{NO}_3)_2$)	>98%
Nickel nitrate ($\text{Ni}(\text{NO}_3)_2$)	>98%
Magnesium oxide (MgO)	>98%

3.2.2 Gases

Gases that are needed in the current work are CH₄ and CO₂ which are available in the gas laboratory (cf. Table 3.2).

Table 3.2 List of gases and its purity

Gases	Purity
Methane (CH ₄)	>98%
Carbon dioxide (CO ₂)	>98%

3.3 Catalysts Preparation

The catalyst was prepared by using co-impregnation method. Firstly, aqueous precursor solutions of Ni(NO₃)₂ and Ce(NO₃)₂ were impregnated together onto MgO with pre-determined concentration in order to obtain the fixed Ni loading of 1 wt% and Ce loadings of 3 and 5 wt%. Then, the precursor solutions were dried overnight over drying temperatures of 120 °C. After drying, the samples were air-calcined in the temperature range of 700 °C.

3.4 Catalyst Characterization

Catalysts characterization techniques may be classified into spectroscopic, morphological, microscopic and physicochemical analysis. The information from various characterizations techniques is essential to investigate the catalytic performance according to the physicochemical attributes. The following section describes the fundamental theory and concepts of various characterization methods used in this work.

3.4.1 Brunauer- Emmett- Teller (BET)

The most commonly used procedure for determination of the surface area of solid materials is the Brunauer-Emmett-Teller (BET) method (Brunauer et al., 1938). It is an extension of the Langmuir's pioneer work (Langmuir, 1916) for monomolecular adsorption. BET equation is derived for multilayer adsorption and based on the relationship between the volume of gas physically adsorbed and the total area of adsorbent, given by:

$$\frac{P}{V(P_s - P)} = \frac{1}{cV_m} + \frac{(c-1)P}{cV_m P_s} \quad (3.1)$$

Where:

P = gas pressure

P_s = saturation pressure of the adsorbate gas

V = volume of gas adsorbed

V_m = volume of gas adsorbed corresponding to monolayer coverage

c = a characteristic constant of the adsorbate

V_m and c may be calculated via the slope and intercept respectively from a linear plot of $V/P (P_s - P)$ against P/P_s . The volume V_m , can then be transformed to the number of molecules adsorbed by using the known value of cross-sectional area of the adsorbent gas molecule. N_2 is the most commonly used adsorbate, which has cross-sectional area of 16.2 \AA^2 . Therefore, the adsorption of N_2 is carried out at the N_2 boiling point of about 77 K. Multi-point BET methods are used to determine the total surface area and pore volume of the catalysts by using Thermo Suffer from Thermo Scientific. The surface area per weight unit can subsequently be computed from

$$S_A = \frac{n_m a_m N}{M} \times 10^{-20} \quad (3.2)$$

Where S_A = surface area of solid (m^2/g)

a_m = average area occupied by a molecule

N = Avogadro's number

M = Molecular weight of adsorbate

n_m = monolayer capacity of adsorbate (g adsorbate /g solid)

Liquid N₂ absorption studies may be used to describe the porosity of powders and other porous materials. The porosity of a solid material can be described through the determination of the total pore volume and pore size distribution. N₂ at 77 K is the most suitable adsorbate to evaluate most of the solid materials. The forces involved in physisorption are the same as those responsible for the condensations of vapors, which include the London dispersion forces and the short-range intermolecular repulsion (Sing and Rouquerol, 1997).

The porosity of a solid material can be understood well from the construction of an adsorption isotherm by measuring the quantity of adsorbate on the surface over a wide range of relative pressures at constant temperature (Sing et al., 1985). Continuous known volumes of N₂ adsorbed by the adsorbent are identified and the equilibrium pressure is measured to obtain the adsorption isotherm point-by-point on the Thermo Suffer. Desorption isotherm can be obtained by measuring the quantities of gas removed from the sample as the relative pressure is lowered.

The total pore volume is determined from the amount of vapour adsorbed at a relative pressure close to unity with the assumption that the pores are then filled with liquid N₂. For the case in which the solid material contains no macropores (pore width > 50 nm), the isotherm will remain nearly horizontal over a range of P/P_0 near the unity (cf. Figure 3.1) and the pore volume is well defined.

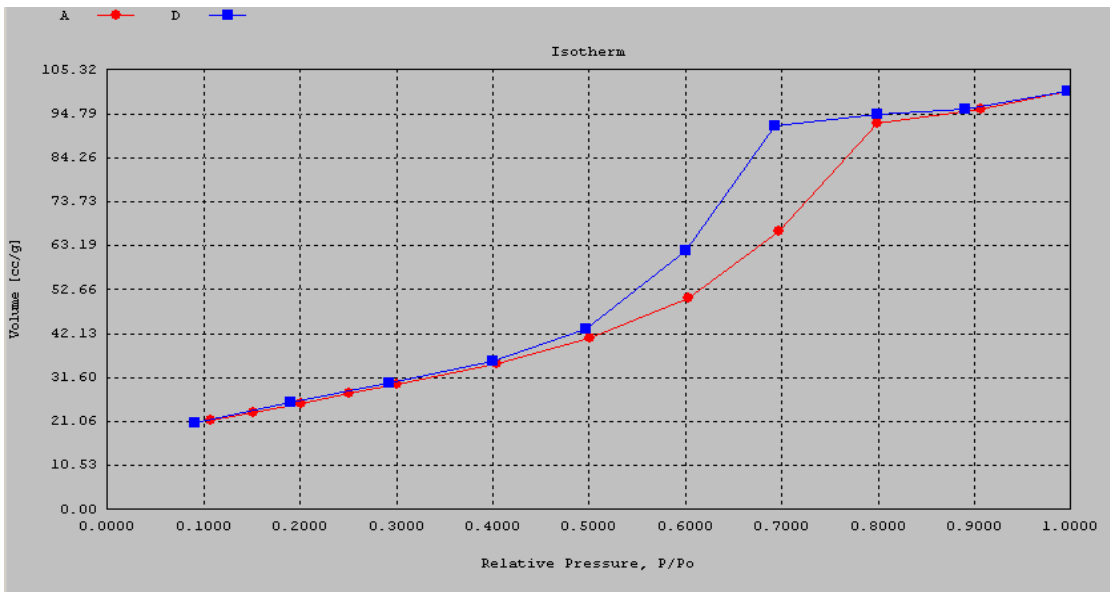


Figure 3.1 Typical N₂ adsorption-desorption isotherms of mesoporous materials

Instead, for macroporous solid material, the isotherm rises rapidly when P/P_0 is in the vicinity of unity. In this case, it may display an essentially vertical rise (cf. Figure 3.2). Thus, the limiting adsorption may be identified with the total pore volume.

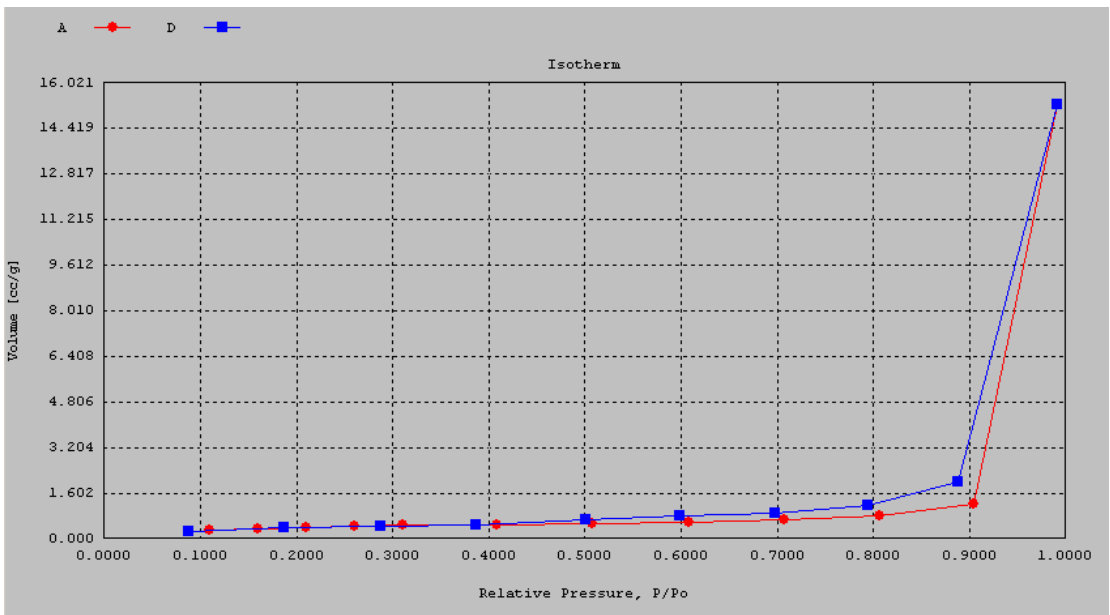


Figure 3.2 Typical N₂ adsorption-desorption isotherms of large macroporous materials.

The volume of nitrogen adsorbed (V_{ads}) can be converted to the volume of liquid N_2 (V_{liq}) contained in the pores by using the following equation:

$$V_{liq} = \frac{P_a V_{ads} V_m}{RT} \quad (3.3)$$

Where P_a and T are ambient pressure and temperature, and V_m is the molar volume of the liquid N_2 ($34.7 \text{ cm}^3/\text{mol}$) respectively.

Since pores which would not be filled below a P/P_o of unity contribute insignificantly to the total pore volume, the average pore size can be estimated from the pore volume. The distribution of pore volume pertaining to pore size is known as a pore size distribution. It is in agreement that the desorption isotherm is more appropriate than the adsorption isotherm for evaluating the pore size distribution of a solid material. The desorption branch of the isotherm reveals a lower relative pressure (P/P_o) resulting in a lower free energy state, and therefore the desorption isotherm is closer to the true thermodynamic stability (Gregg and Sing, 1982). Nitrogen molecules tend to be adsorbed on pore walls through a multilayer film at lower pressure while nitrogen molecules fill the pores through capillary condensation mechanism at higher pressure. Mesopore size calculations are implemented by assuming cylindrical pore geometry using the Kelvin equation (Gregg and Sing, 1982):

$$r_k = \frac{-2\gamma V_m}{RT \ln\left(\frac{P}{P_o}\right)} \quad (3.4a)$$

Where

P/P_o = relative pressure of N_2

R = gas constant ($8.314 \text{ E7 ergs/K.mol}$)

T = N_2 boiling point (77 K)

γ = surface tension of N_2 at its boiling point (8.85 ergs.cm^2 at 77K)

V_m = molar volume of liquid N_2 ($34.7 \text{ cm}^3/\text{mol}$)

r_k = the Kelvin radius of the pore

Using the appropriate constants for N_2 , the equation (3.4a) reduces to:

$$r_k(A) = \frac{4.15}{\lg\left(\frac{P}{P_o}\right)} \quad (3.4b)$$

The Kelvin radius is defined as the radius of the pore in which condensation happens at P/P_o . However, r_k does not represent the actual pore radius because some adsorption has taken place before condensation happens on the walls of the pore. Moreover, there is an adsorbed layer remained on the walls during desorption when evaporation occurs.

As a result, the actual pore radius (r_p) is given by:

$$r_p = r_k + t \quad (3.5)$$

Where t is the thickness of the adsorbed layer. The t -value can be estimated by a method proposed by (de Boer et al., 1966) as:

$$t(A) = \left(\frac{13.99}{\lg\left(\frac{P}{P_o}\right) + 0.034} \right)^{1/2} \quad (3.6)$$

AS1 WIN computes the pore size distribution by using the methods proposed by Barrett, Joyner, and Halenda (BJH) (Barrette et al., 1951) and by Dollimore and Heal (DH) (Dollimore and Heal, 1964). However, the BJH method is the most extensively used method for the estimation of the pore size distribution (Sing and Rouquerol, 1997). The BJH procedures are based on the emptying of the pores by a step-wise reduction of P/P_o , and the derived pore size distribution is normally expressed in the graphical form of $(\delta V_p / \delta r_p)$ versus r_p or d_p . However, Horvath and Kavazoe method is used to determine the pore size distribution of the samples for this research.

3.4.2 X-ray Photoelectron Spectroscopy (XPS)

XPS provides information on element composition (except H and He), molecular environment (oxidation state and bonding atoms), non destructive elemental depth profiles 10nm into the sample and the dispersion of one phase over another. Binding energy contains chemical information because the energy levels of core electrons depend slightly on the chemical state of the atom. Normally, the binding energy increases with increasing oxidation state.

XPS was carried out on a JPS-9010 instrument to study the composition of deposited films by ionizing surface atoms and measuring the energy of ejected photoelectrons. Ni/MgO catalyst specimen (in spherical form) will be bombarded with low energy X-rays source of Al K α (1486.3 eV). The X-rays will help to eject photoelectrons with binding energy, E_b from either valence or inner core electron shell when an atom absorbs a photon of energy, $h\nu$. The kinetic energy of the photoelectron, E_k , is given by Eq. (3.7).

$$E_k = h\nu - E_b - \Phi \quad (3.7)$$

Where E_k is the kinetic energy of the photoelectron, h is Planck's constant, ν is frequency of the exciting radiation, E_b is the binding energy of the photoelectron with respect to the Fermi level of the sample and ϕ is the work function of the spectrometer. The identity of the atom from which the electron comes from can be determined from the binding energy of the ejected electrons. Usually, the analysis is carried out under ultra-high vacuum ($< 10^{-10}$ Torr) to prevent surface contamination.

As illustrated by Figure 3.3, X-ray is pointed onto the sample and the resulting photoelectrons are then focused onto the entrance slit of a concentric hemispherical analyzer. A negative and positive potential are applied to the outer and inner cylinders, respectively, such that the central line between the cylinders is a line of zero potential. The potentials are scanned to control the energy of electrons that are allowed to pass through the analyzer and onto the detector, usually a channel electron multiplier (channeltron).

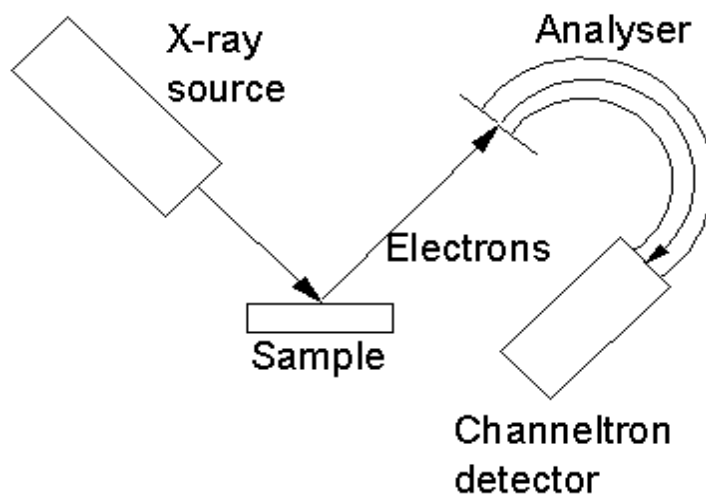


Figure 3.3 Schematic diagram of a XPS apparatus

3.4.3 X-ray Diffraction (XRD)

XRD is a non-destructive analytical technique used to identify the structure, crystalline phases and also the size of crystallites of natural or synthetic materials. The amount of sample used for this analysis requires only a few milligrams and the samples can be in the form of powders, solids, films or ribbons. Nevertheless, it is more accurate if the sample used is up to few grams. The variation of XRD patterns also known as “fingerprint” depends on the internal structure of the material and therefore the characteristics can be identified.

The sample mean crystallite size ranged from 3 to 50 nm can be estimated by using this technique. For the crystallite size smaller than 3 nm, the diffraction lines of X-ray pattern would be broad, diffused or even absent. However, the change in shape of the line would not be apparent for crystallite size larger than 50 nm (Anderson and Pratt, 1985). Therefore, the application of XRD is limited in two ways. Firstly, it cannot detect amorphous phases and secondly, optimum analysis may be achieved when the crystallite size is within the effective regime (3 to 50 nm).

In XRD analysis, the sample is polished to powder so that all possible orientations of the crystal structure to the X-ray beam can be demonstrated. When X-ray beam with wavelength, λ is incident on the crystalline structure, diffraction occurs due to interference caused by the nature of the material. The angle at which constructive interference occurred is measured and subsequently the interplanar distances, “d-spacings” between the crystal lattice is determined from Bragg equation (Cullity, 2001). The interplanar spacings depend solely on the dimension of the crystal’s unit cell. On the other hand, the intensities of the diffracted rays function as the placement of the atoms in the unit cell (Klug and Alexander, 1974). Bragg formula is given by Eq. (3.8).

$$n\lambda = 2d \sin \theta \quad (3.8)$$

where n is the order of reflection (integer), λ is wavelength of X-ray beam (nm), d is interplanar distances of crystal (d-spacing) and θ is angle of incidence (degrees).

With the assumption that the diffraction line shapes are Gaussian, the squares of the contributing width factors are additive. The line width due to particle size broadening can be defined by using Eq. (3.9).

$$\beta_d^2 = \beta_{obs}^2 - \beta_{inst}^2 \quad (3.9)$$

Where β_d is true line width at half maximum intensity (degree), β_{obs} is observed width at half maximum intensity (degree) and β_{inst} is instrumental line width by standard (degree). β_{inst} is obtained from a calibration process using a standard of high quality with a crystalline size greater than 1000 Å. From the results, the mean crystallite size will be calculated by the Scherrer equation, (Liebhafsky et al., 1972).

$$D = \frac{k_{sch}\lambda}{\beta_d \cos \theta} \quad (3.10)$$

where D is the crystalline size (nm), λ is wavelength of X-ray (nm), β_d is angular width at half maximum intensity (radian), θ is Bragg's angle (degree) and k_{Sch} is Scherrer constant and equals to 0.93 (Warren, 1969).

The schematic diagram of XRD is presented in Figure 3.4, XRD measurements will be carried out on a Philips X' Pert system using $\text{CuK}\alpha$ ($\lambda = 1.542 \text{ \AA}$) at 30 kV and 15 mA. Initially, the sample is milled to fine powder for the purpose of revealing all possible orientations of the crystal structure to the x-ray beam. It is then placed on a glass specimen holder and pressed by using a glass slide. The X-rays are first generated by a cathode ray tube, filtered to produce monochromatic radiation, collimated to be directed towards sample. The interaction of the incident rays with the sample produces constructive interference. The diffracted x-rays are then detected, processed and counted. The sample is scanned from 20° to 90° at a speed of $1^\circ/\text{min}$, and all the possible diffraction directions of the lattice in theory should be attained. The conversion of the diffraction peaks to d-spacings based on International Centre for Diffraction Data (ICDD) database search match interpretation method allows the identification of the type of phases present.

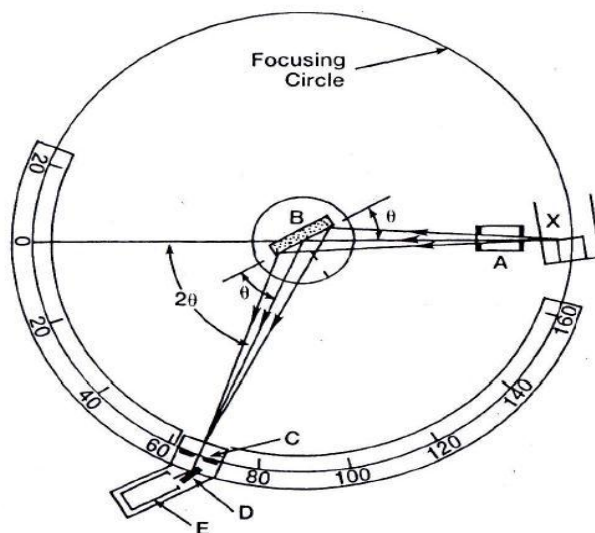


Figure 3.4 Schematic diagram of XRD (A) Collimation (B) Sample (C) Slit (D) Exit Beam Monochromator (E) Detector (X) Source of X-Rays (Cullity, 1978).

3.4.4 Field Emission Scanning Electron Microscopy-Energy Dispersive X-ray (FESEM-EDX)

Field Emission Scanning Electron Microscopy (FESEM) is a non-destructive analysis technique that shows the information such as sample morphology or texture, sample topography, sample composition, crystalline structure and orientation of materials which contribute to the structure of the sample from electron-sample interactions by directing a beam of high energy electrons to produce a variety of electrons emitted from surface of the sample (Histopathology, 1973). Figure 3.6 illustrates the schematic diagram of FESEM. A detector is used to catch the secondary electrons and create an image of the sample surface by measuring the secondary electrons intensity as a function of the position of the scanning primary electron beam. The image is then displayed on a monitor. A 3- dimensional image can be obtained by collecting data from a selected area of the surface of the specimen. When electrons accelerate in FESEM, they carry a significant amount of kinetic energy produced by electrons-sample interactions which are subsequently dissipated as signals. These signals involve secondary electrons which generate the FESEM images (morphology and topography of samples), backscattered electrons (BSE) and diffracted backscattered electrons (Michler, 2004).The intensity of the backscattered electrons generated by electron bombardment can be correlated to the atomic number of the element within the sampling volume. The distinctions of the images are caused by the difference in electron collection efficiency which depends on the angle of emission, atomic number of elements and surface relief (Bergeret and Gallezot, 1997).Energy Dispersive X-ray (EDX) usually comes with field emission scanning microscopy analysis (FESEM) for better analysis results. Same equipment shown in Figure 3.5 will be used for both FESEM and EDX with the same parameters.

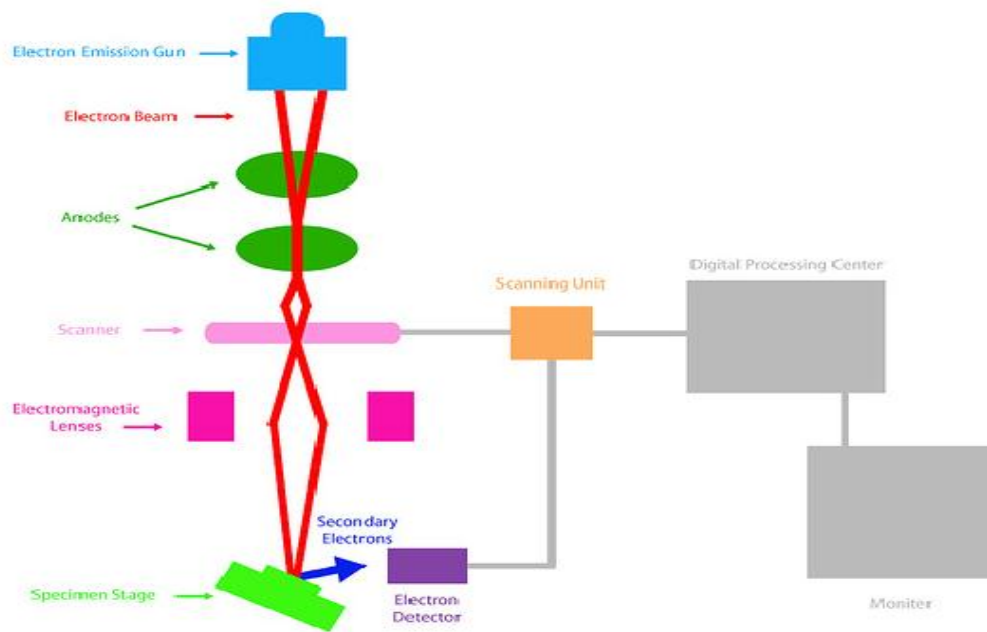


Figure 3.5 Schematic diagram of FESEM

3.4.5 Thermogravimetric Analysis (TGA)

TGA is a technique employed to measure weight changes of a sample when subjected to linear thermal programming. The importance of TGA is that it provides information such as composition, thermal stability, oxidative stability, decomposition kinetics and estimated life time of the sample. The weight of the sample is monitored as a function of temperature or time when the sample specimen is subjected to linear thermal programming. Depending on the nature of the reaction, a new species may be formed which may lead to either increase or decrease in sample weight. The changes in weight of the sample are attributed to decomposition, oxidation and reduction of the sample upon heating. The measurement of the changes in sample weight is usually carried out in air or an inert atmosphere. The usual gasifying agents used in TGA are pure oxygen, air and nitrogen. The temperature setting in TGA depends on the thermal stability of the sample. Typical heating rates employed in TGA measurements are in the range of 10-20 °C/min. The sample used for measurement in TGA should be in small amount and approximately 5mg of samples are recommended.

3.4.5.1 Calcination

Figure 3.6 shows the principle of TGA. TGA was carried out over 3 uncalcined catalyst samples. Approximately 5 mg catalyst samples were placed in a quartz boat micro-statically balance in a counter current flow of gasifying agent. Air was chosen as a gasifying agent. The temperature was fixed till 900 °C. 3 different heating ramps of 10 °C/min, 15 °C/min and 20 °C/min were used in the analysis. During temperature ramping, metal nitrate decomposed to give corresponding oxides. Due to the release of NO₂, weight loss of the sample occurred with time-on-stream. A computer controlled data acquisition program was used to monitor the weight and temperature changes during the process.

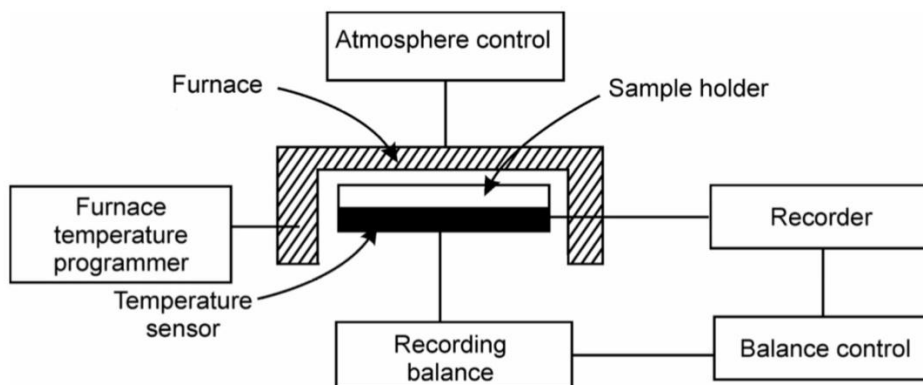


Figure 3.6 Schematic diagram of TGA

3.4.5.2 Non-isothermal Thermogravimetric Analysis

The carbon gasification experiment was carried out in a TGA unit using 5mg of the coked sample in a quartz boat micro-statically balance in a counter current flow of gasifying agent. In this case, O₂ was used as the gasifying agent. Coked catalyst was gasified with O₂ at heating ramp 10 °C/min to 900 °C. It was a non-isothermal carbon solid reaction. The maximum temperature was fixed till 900 °C to ensure that the carbon deposited on the catalyst was removed completely without sintering of catalyst. To provide intimate gas-solid contact in the TGA unit, the O₂ flow rate was metered at 50ml /min. A computer controlled data acquisition program was used to monitor the change in

weight and temperature during the process. TGA technique allows the coke location on the supported metal catalyst to be determined by observing the peaks that occurred.

3.5 Catalyst Testing

Figure 3.7 shows the experiment setup for the catalysts testing. The catalytic evaluation was carried out by placing 0.30g of catalyst into the quartz glass fixed-bed reactor (ID: 10 mm) supported by two layers of quartz wool. Digital flow controller was used to meter CO₂ and CH₄ into the reactor. Catalyst screening was carried out using feed mixture of the CH₄ and CO₂ in equal proportion and the reaction temperature was set at 1073 K. The reaction temperature was then varied to 1123 K and 1173 K to determine the effect of temperature on the H₂/CO ratio in the synthesis gas for the best catalyst. The composition of synthesis gas produced was determined by using online Agilent 3000 micro-gas chromatography (GC) with TCD column, Backflush Molecular Sieve 5A and Plot U column.

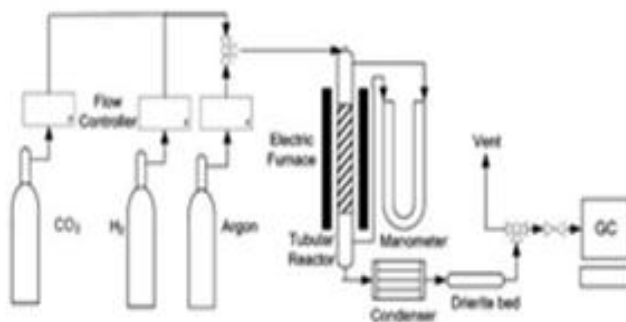


Figure 3.7 Experimental setup of catalyst testing

CHAPTER 4 RESULTS AND DISCUSSION

4.1 Fresh Catalyst Characterization

4.1.1 XRD Diffraction Pattern

The crystalline phase of 5 wt% Ce-Ni/MgO was identified by using XRD techniques. XRD is a non-destructive analytical technique which is widely used to identify the crystalline structure, crystalline phase and also the size of crystallites of natural or synthetic materials. Figure 4.1 shows the XRD patterns for 5wt% Ce-Ni/MgO catalyst whereas Table 4.1 shows the summary of values of 2θ , intensity, inter plane distance of crystal (d-spacing) and crystallite size for the diffraction peaks.

From Figure 4.1, XRD patterns show the effect of Ce addition to the catalyst as the peaks appeared at $2\theta = 28.53^\circ$ and 47.46° . The peak at $2\theta = 37.00^\circ$ corresponds to MgO whereas the peaks at 42.99° , 62.41° , 74.84° and 78.79° correspond to NiO. At around $2\theta = 42.99^\circ$, the peak has sharp intensity indicating that the catalyst has good crystallinity (cf. Figure 4.1). In contrast, amorphous phase is not present.

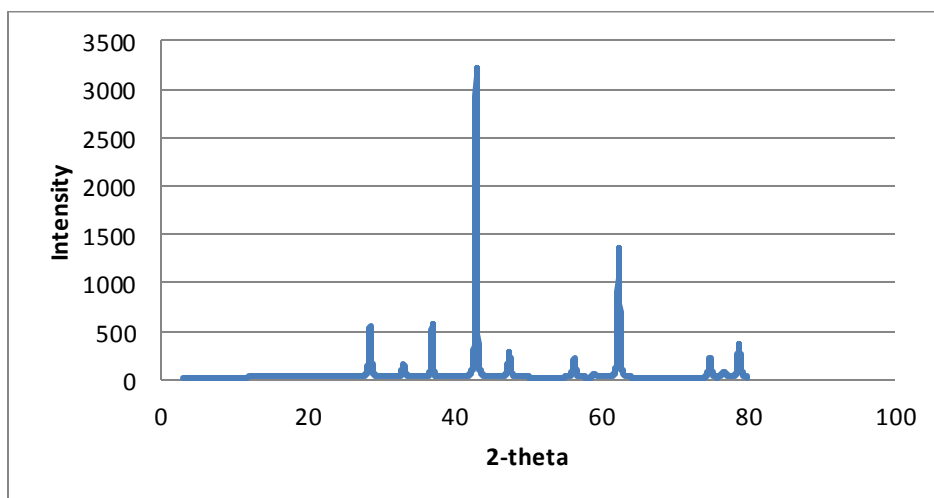


Figure 4.1 XRD patterns for 5 wt% Ce-Ni/MgO catalyst

Table 4.1 Summary of values of 2θ , intensity, inter plane distance of crystal (d-spacing) and crystallite size for the diffraction peaks

2θ (degree)	Intensity	d (ang)	Crystallite size
28.53	551.29	3.16	242
33.05	166.02	2.70	236
37.00	577.64	2.43	429
42.99	3209.36	2.10	417
47.46	278.66	1.91	243
56.36	225.01	47.46	256
59.06	55.18	56.36	186
62.41	1352.44	1.49	398
74.84	219.14	1.27	331
76.76	85.19	1.24	241
78.79	373.86	1.21	370

4.1.2 Liquid N₂ Physisorption

The textural properties of the fresh Ce-Ni/MgO catalysts were characterized using liquid N₂ physisorption technique. Figures 4.2 and 4.3 show the isotherm plot of Ce-Ni/MgO catalysts with 3 wt% and 5 wt% Ce loadings respectively. The hysteresis pattern has conclusively shown that the catalysts are mesoporous materials.

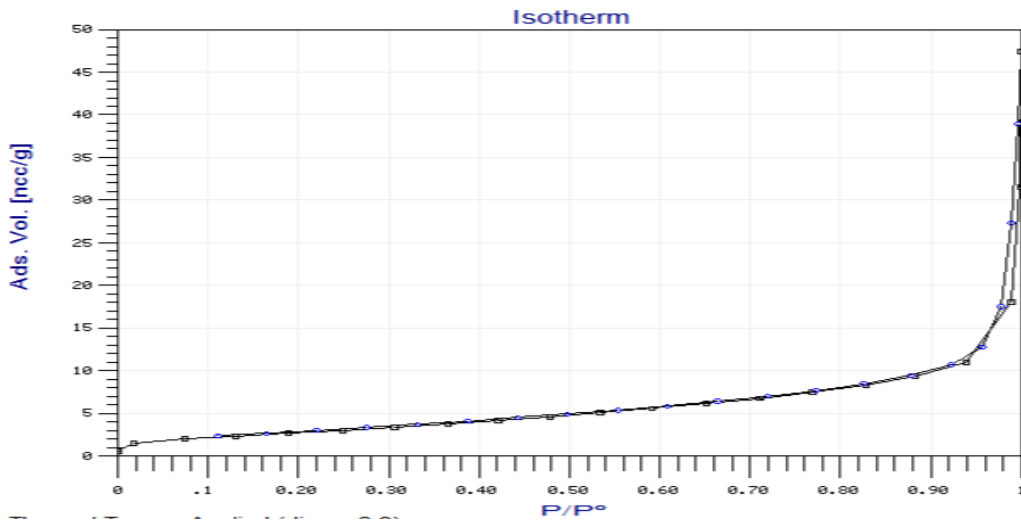


Figure 4.2 Isotherm plot for 3 wt% Ce-Ni/MgO catalyst

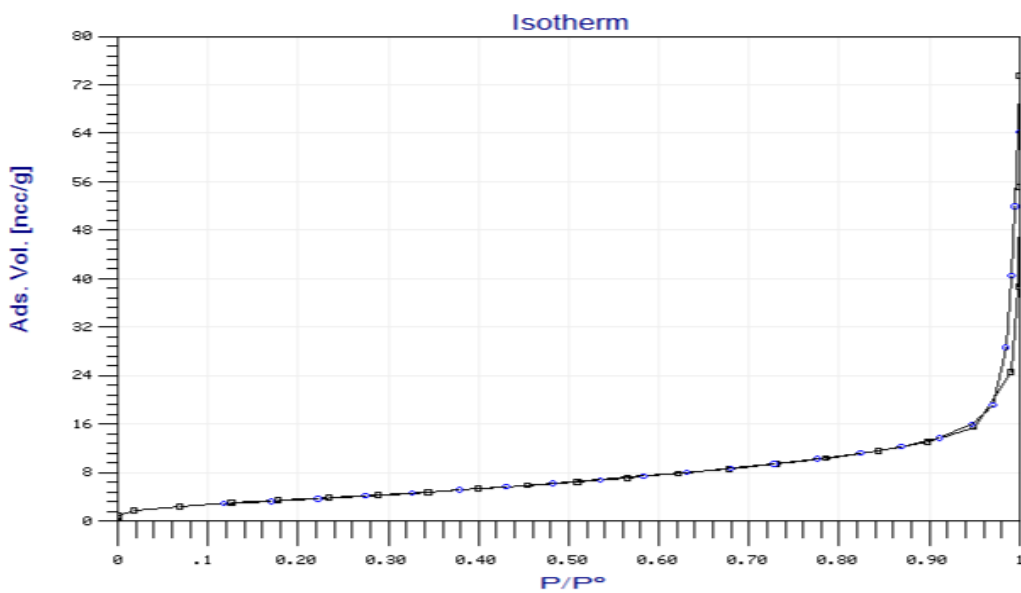


Figure 4.3 Isotherm plot for 5 wt% Ce-Ni/MgO catalyst

Table 4.2 shows that the 5 wt% Ce-Ni/MgO catalyst has larger BET specific surface area than the 3 wt% Ce-Ni/MgO catalyst. It shows that the nickel metal is well dispersed on the MgO support even with the increased Ce loadings. In addition, pore volume and pore diameter of 5 wt% Ce-Ni/MgO catalyst are slightly larger than that of 3 wt% Ce-Ni/MgO catalyst.

Table 4.2 BET specific surface area, pore volume and pore diameter of the catalyst samples

Samples of catalysts (wt% Ce)	BET specific surface area (m^2g^{-1})	Pore volume (cm^3g^{-1})	Pore diameter (nm)
3	10.59	0.0035	0.88
5	14.00	0.0045	0.96

4.1.3 FESEM Imaging

The topography and morphology of fresh catalyst was further studied by FESEM. Figure 4.4 shows that the metallic particles in 5 wt% Ce-Ni/MgO catalyst are uniformly distributed.

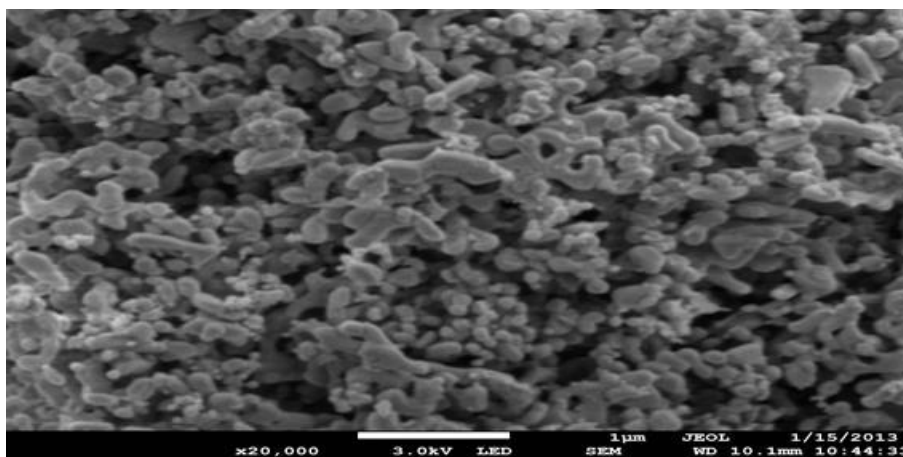


Figure 4.4 SEM image of 5 wt% Ce-Ni/MgO catalyst

4.1.4 EDX

Figure 4.5 shows the quantification of the atomic elements contained in the 5 wt% Ce-Ni/MgO catalyst in terms of atomic percentage concentration. The concentrations of the elements Mg and O are attributed to the MgO support of the catalyst. The elements of Ni and Ce are also detected. Their weight percentages are 23.49 wt% and 3.46 wt% respectively. A small quantity of carbon is found for the catalyst, which contributes the weight percentage of 2.81 wt% to the catalyst. It proves that addition of Ce as promoter can reduce the carbon deposition on the catalyst effectively. Ce has high O₂ storage capability; therefore carbon deposited on the catalyst will tend to react with O₂ to form CO₂ and thus a large amount of carbon is removed from the catalyst surface (Daza et al., 2010).

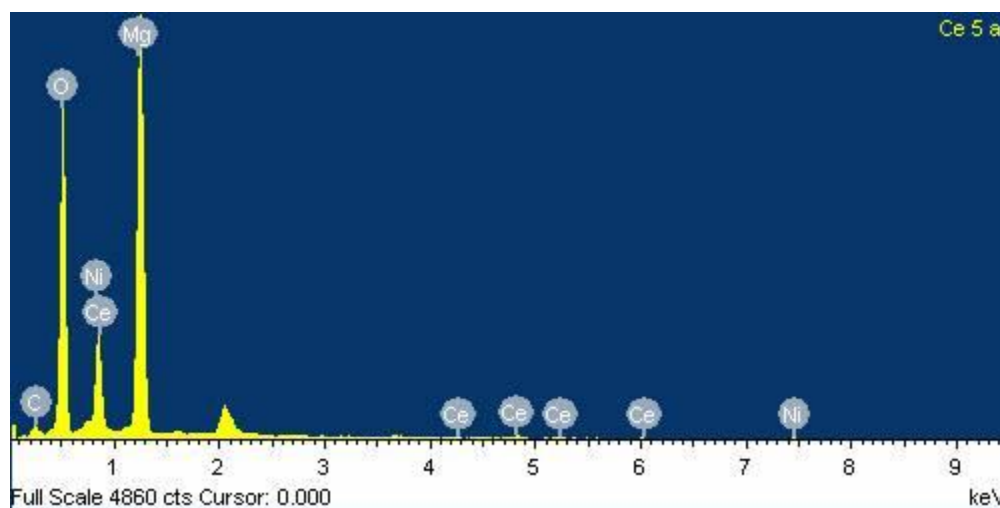


Figure 4.5 EDX of 5 wt% Ce-Ni/MgO catalyst

4.1.5 Thermogravimetric Analysis (TGA)

From the result obtained for each catalyst, the existence of small peaks at the temperatures below 200°C was due to the water elimination from the catalyst whereas the peak hovered in between 330°C and 360°C was attributed to the $\text{Ni}(\text{NO}_3)_2$ decomposition into NiO. For each heating ramp, there are slight changes of the maximum peak when 5% Ce are promoted to Ni/MgO catalysts. Figures 4.6 and 4.7 show the graphs of derivative weight versus peak temperature for dry Ni/MgO catalyst and 5% Ce-Ni/MgO catalyst respectively at the heating ramp of 10°C/min. For the heating ramp of 10°C/min, 5% Ce-Ni/MgO catalyst gives a slightly higher peak compared to Ni/MgO catalyst. It means that the extent of decomposition of $\text{Ni}(\text{NO}_3)_2$ into NiO is greater with the promotion of Ce to the catalyst.

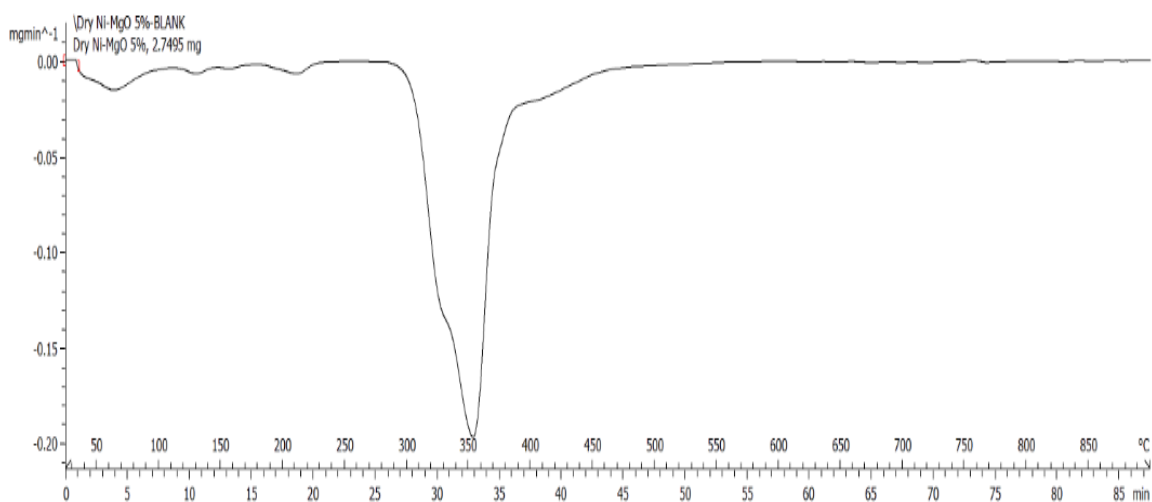


Figure 4.6 Graph of derivative weight versus peak temperature for Ni/MgO catalyst at the heating ramp of 10°C/min

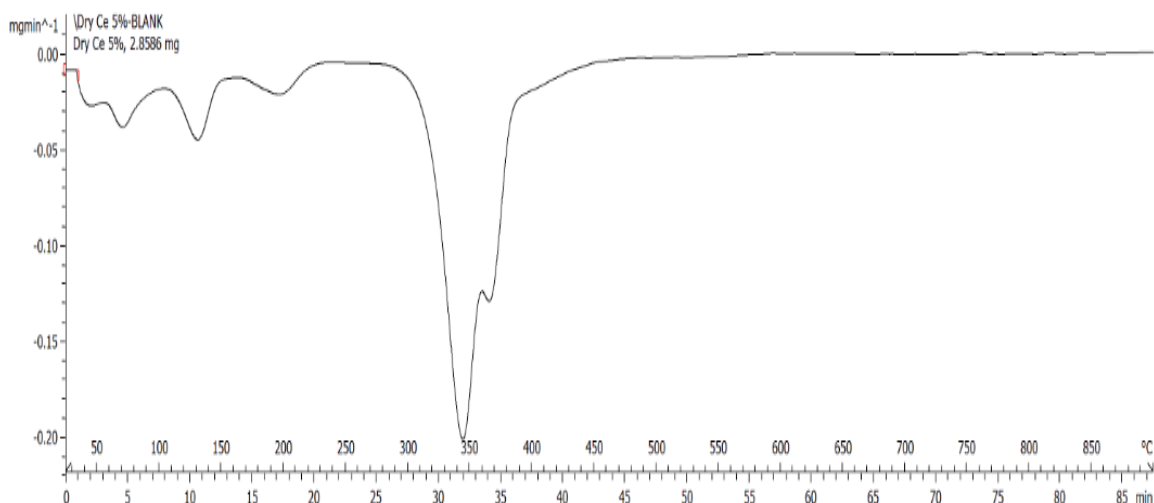


Figure 4.7 Graph of derivative weight versus peak temperature for 5wt% Ce-Ni/MgO catalyst for the heating ramp of 10°C/min

Three different heating ramps viz. 10°C/min, 15 °C/min and 20 °C/min were used for temperature-programmed calcinations studies to investigate the gas-solid interaction during the calcinations and to determine the calcination temperatures for the catalysts that were subsequently employed in the reaction. Figures 4.8 and 4.9 show the graphs of derivative weight versus peak temperature for 5 wt% Ce-Ni/MgO catalyst at the heating ramps of 15 °C/min and 20 °C/min respectively. It is observed that when the heating ramp increases, the magnitude of the highest peak becomes higher. When the heating rate increases, the highest peak has also shifted to the higher temperature range. This trend was in agreement with the Kissinger proposition and hence can be adequately captured by the model-free Kissinger equation.

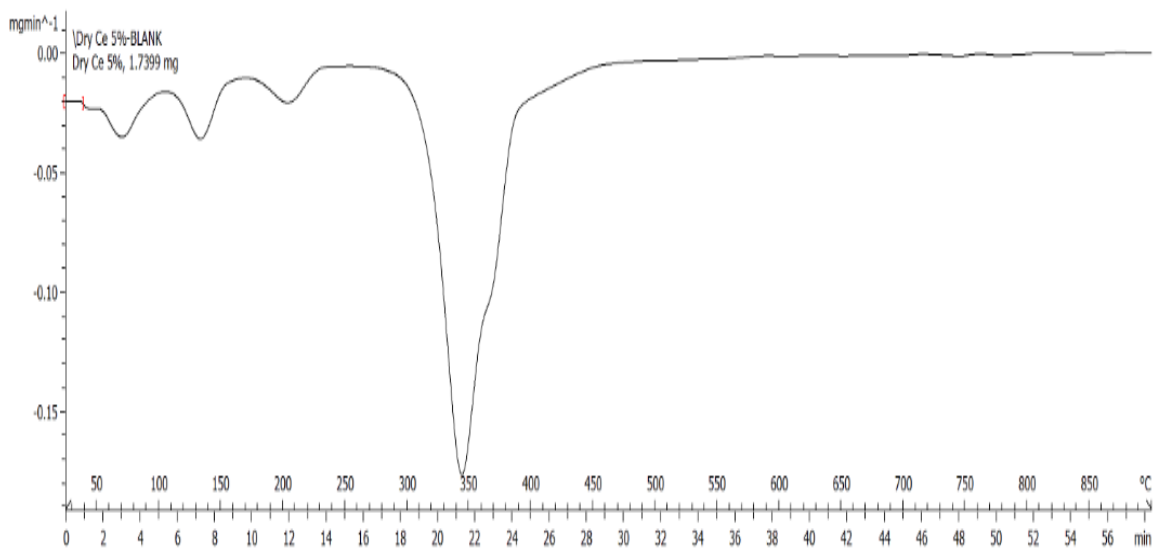


Figure 4.8 Graph of derivative weight versus peak temperature for 5wt% Ce-Ni/MgO catalyst for the heating ramp of 15°C/min

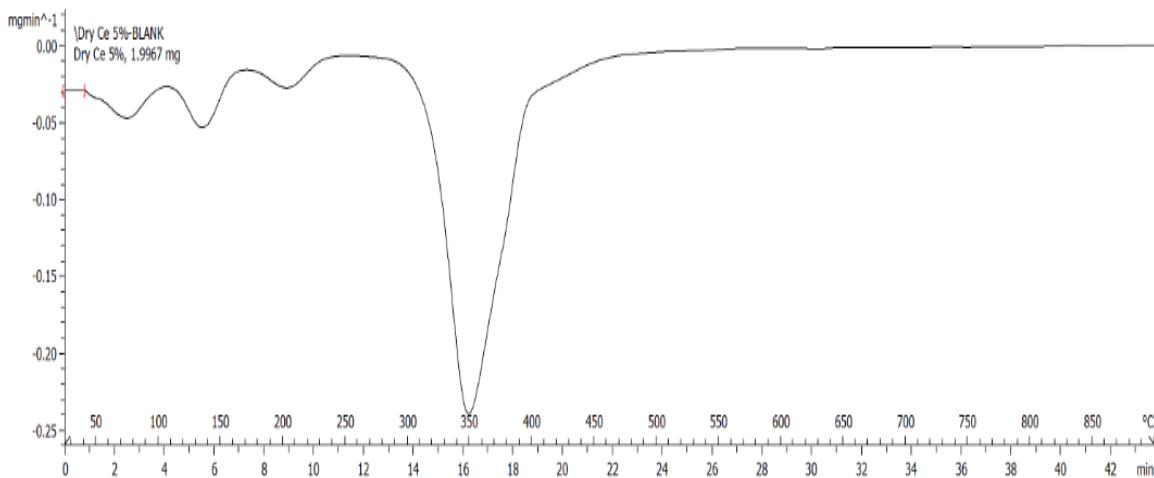


Figure 4.9 Graph of derivative weight versus peak temperature for 5wt% Ce-Ni/MgO catalyst for the heating ramp of 20°C/min

Table 4.3 lists the maximum peak temperature for two uncalcined catalyst samples at three different heating ramps.

Table 4.3 Different heating ramps and maximum peak temperature for two uncalcined catalyst samples.

Sample (wt% Ce)	Heating ramps (°C/min)		
	10	15	20
0	355	360	365
5	345	348	350

The activation energy values associated with calcination procedures of all catalyst samples were subsequently obtained by using Kissinger model. Kissinger model proposes that a plot of $\ln(\frac{\beta}{T_p^2})$ versus $\frac{1}{T_p}$ will produce a straight line from which the activation energy of the catalyst can be determined where by β and T_p represent the heating ramp and maximum peak temperature respectively. Figure 4.10 shows the resulting modeling of the catalyst samples.

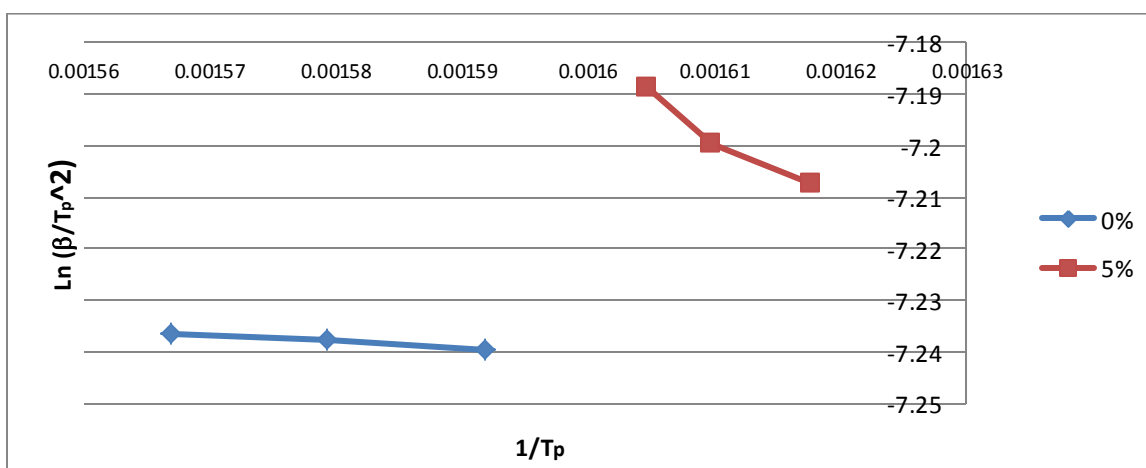


Figure 4.10 Kissinger model for two different catalysts

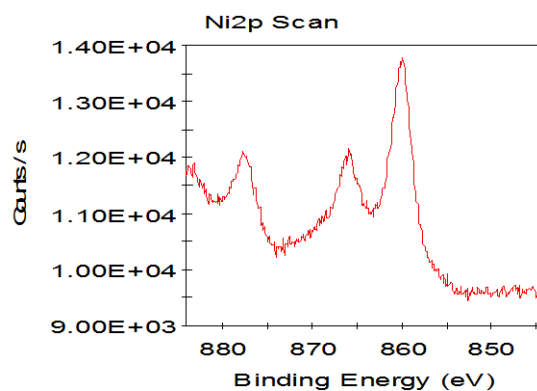
Table 4.4 summarizes the activation energies of Ni/MgO and 3%-Ce-Ni/MgO catalysts during calcination. It was obvious that 5% Ce-Ni/MgO catalyst has much higher activation energy than Ni/MgO catalyst. It showed that Ce-Ni/MgO is highly stable due to the stronger metal-metal interactions in the catalyst.

Table 4.4 Activation energies of catalyst samples

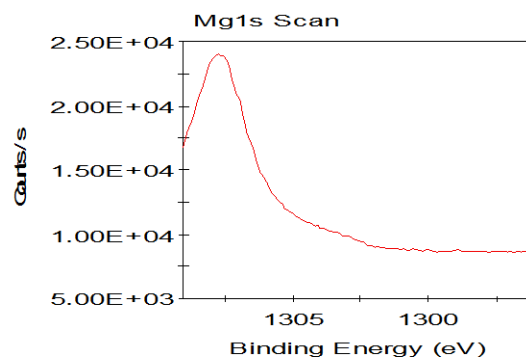
Sample (wt% Ce)	E_a (J/mol)	R^2
0	1038.93	0.9992
5	11904.83	0.9571

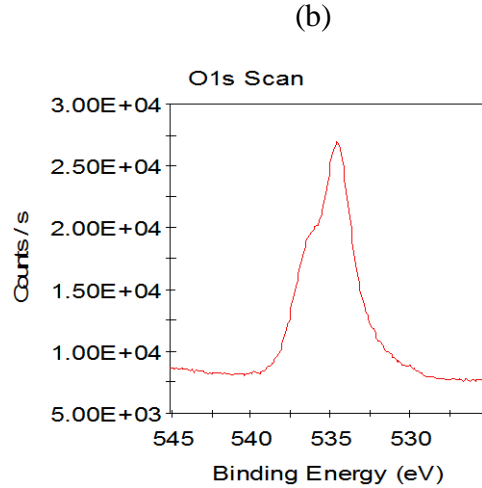
4.1.6 X-ray Photoelectron Spectroscopy (XPS)

Figure 4.11 shows XP spectra of Ni2p, Mg1s and O1s of fresh Ni/MgO catalyst. Table 4.5 lists the binding energy of each element in the catalyst and their corresponding counts per unit second. Ni2p can be deconvoluted in three components centered at 859.98, 868.88 and 877.68 eV. The three components can be assigned with Ni⁰ and Ni²⁺ probably as NiO or Ni(OH)₂ due to the asymmetry of the signals. The main signal at 1307.78 eV corresponds to Mg1s associated with MgO. The signal at 534.58 eV refers to the existence of O1s element in the catalyst. It is associated with the formation of NiO and MgO.



(a)





(c)

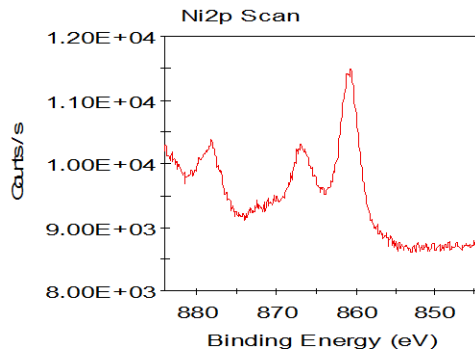
Figure 4.11 XP spectra of (a) Ni2p (b) Mg1s (c) O1s of fresh Ni/MgO catalyst

Table 4.5 Binding energies of each element in fresh Ni/MgO catalyst and their corresponding count per unit second

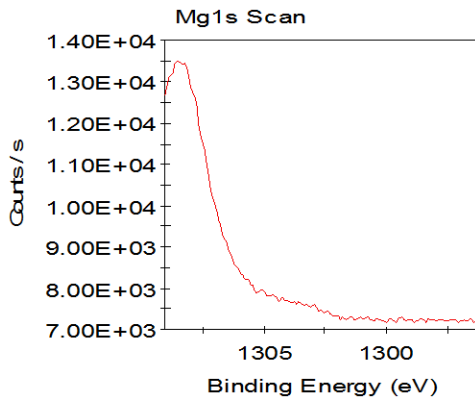
Elements		Binding energy (eV)	Counts /s
Ni2p	Start	844.08	9685.64
	Peak	859.98	13719.6
	End	884.08	11755
Mg1s	Start	1296.08	8603.51
	Peak	1307.78	24066.9
	End	1309.08	16717.4
O1s	Start	525.08	7633.5
	Peak	534.58	26924.5
	End	540.08	8599.98

Figure 4.12 shows XP spectra of Ni2p, Mg1s, O1s and Ce3d of fresh 3wt% Ce-Ni/MgO catalyst. Table 4.6 lists the binding energies of each element in the catalyst and their corresponding counts per unit second. For this catalyst, the three components deconvoluted at 860.58, 866.88 and 878.18 eV correspond to Ni⁰ and Ni²⁺ probably as

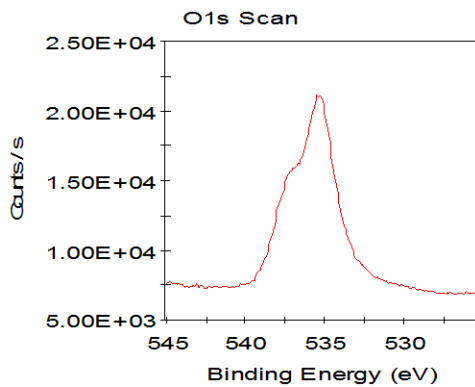
NiO or Ni(OH)₂ due to the asymmetry of the signals. The presence of Mg1s at 1308.48 eV is associated with MgO. The main signal at 535.48 eV refers to O1s which is the element of NiO or MgO in the catalyst. The deconvolution of Ce3d at 878.08, 887.18, 903.98 and 921.88 eV can be associated with the presence of Ce³⁺ and Ce⁴⁺. However, Ce is mostly found as Ce⁴⁺ in mixed oxide.

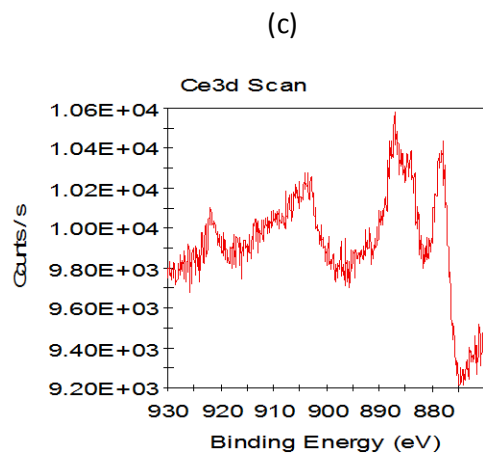


(a)



(b)





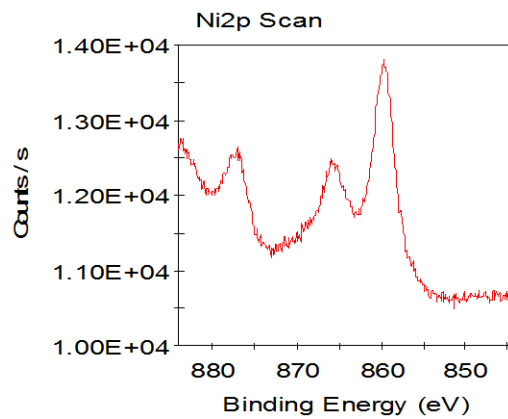
(d)

Figure 4.12 XP spectra of (a) Ni2p (b) Mg1s (c) O1s (d) Ce3d of fresh 3wt% Ce-Ni/MgO catalyst

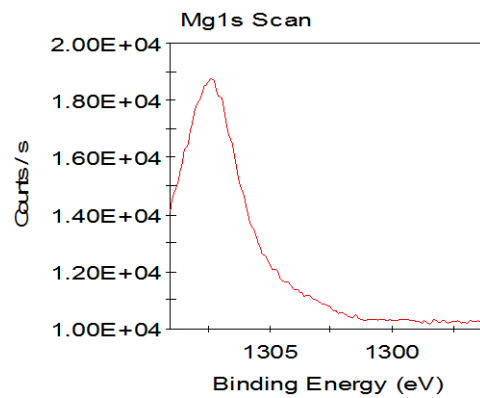
Table 4.6 Binding energies of each element in fresh 3wt% Ce-Ni/MgO catalyst and their corresponding counts per unit second

Elements		Binding energy (eV)	Counts /s
Ni2p	Start	844.08	8793.54
	Peak	860.58	11496.5
	End	884.08	10199
Mg1s	Start	1296.08	7150.09
	Peak	1308.48	13499.1
	End	1309.08	12690.6
O1s	Start	525.08	6943.08
	Peak	535.48	21134.1
	End	545.08	7536.16
Ce3d	Start	870.08	9470.93
	Peak	887.18	10578.4
	End	930.08	9750.46

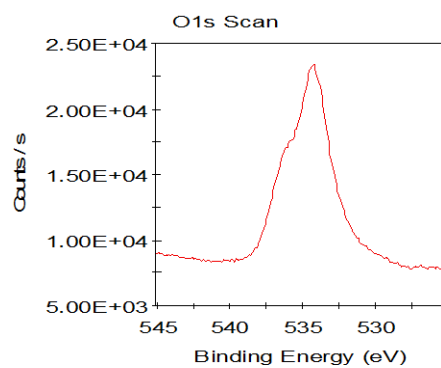
Figure 4.13 shows XP spectra of Ni2p, Mg1s, O1s and Ce3d of fresh 5wt% Ce-Ni/MgO catalyst. Table 4.7 lists the binding energies of each element in the catalyst and their corresponding counts per unit second. Ni2p is deconvoluted into three components located at 859.68, 866.08 and 877.08 eV. The three components are associated with Ni⁰ and Ni²⁺ probably as NiO or Ni(OH)₂ due to the asymmetry of the signals. The binding energy of 1307.38 eV in Mg1s spectrum corresponds to Mg²⁺ in MgO support. O1s element at 535.48 eV relates to O²⁻ found in the formation of NiO or MgO. In Ce3d spectrum, main signals are observed at 876.98, 885.78, 902.98 and 920.78 eV. The main signals can be explained by the presence of Ce³⁺ and Ce⁴⁺ in the catalyst. However, the amount of Ce⁴⁺ is larger than that of Ce³⁺ in the catalyst.



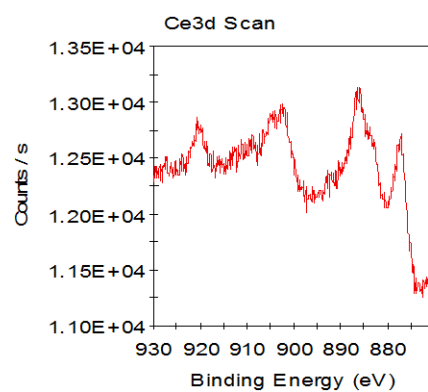
(a)



(b)



(c)



(d)

Figure 4.13 XP spectra of (a) Ni2p (b) Mg1s (c) O1s (d) Ce3d of fresh 5wt% Ce-Ni/MgO catalyst

Table 4.7 Binding energies of each element in fresh 5wt% Ce-Ni/MgO catalyst and their corresponding counts per unit second

Elements		Binding energy (eV)	Counts /s
Ni2p	Start	844.08	10712.1
	Peak	859.68	13797.1
	End	884.08	12676.6
Mg1s	Start	1296.08	10200
	Peak	1307.38	18742.9
	End	1309.08	14134.6
O1s	Start	525.08	7808.28
	Peak	534.28	23349.3
	End	545.08	9005.32
Ce3d	Start	870.08	11493.3
	Peak	885.78	13139.1
	End	930.08	12347.7

4.2 Dry Reforming Reaction Studies

4.2.1 Catalyst Screening

For the catalyst screening process, feed comprised of the CH₄ and CO₂ mixture at equal proportion was employed and the reaction temperature was set at 1123 K. Figure 4.14 shows the influence of Ce loading on rate of formation of product yield. For all the runs, it can be observed that 3 wt% and 5 wt% Ce-Ni/MgO catalysts gave almost equal rate of formation of product yield (H₂ and CO). Compared to unpromoted Ni/MgO catalyst, both Ce-promoted catalysts yielded significant improvement in the methane dry reforming rate. Moreover, while the unpromoted Ni/MgO produced H₂:CO at a ratio lower than unity, the ratio of H₂ to CO has increased to more than unity when Ce was loaded (for both 3wt % and 5 wt%). This indicates that not only Ce has improved the reactivity of the catalyst, it offers an additional role of providing an alternative pathway that can enhance the H₂:CO

ratio, most likely the enhancement of CH₄ cracking to produce more H₂. This is consistent with the conversion profile captured in Figure 4.15.

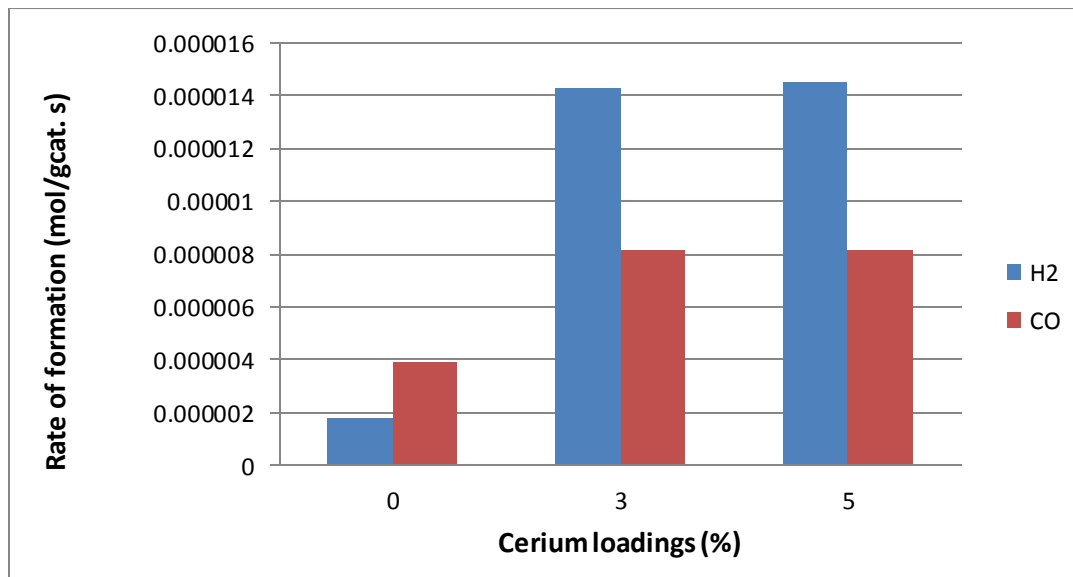


Figure 4.14 Rate of formation of both H₂ and CO for Ni/MgO catalysts with different Ce loadings at 1123K and CH₄/CO₂ ratio of 1:1

The CH₄ conversion over the Ni/MgO catalyst with various cerium loadings was also determined. Figure 4.15 illustrates the variation of CH₄ conversion with various cerium loadings at the first and second hour of the reaction. As can be observed from Figure 4.15, an increment in Ce loading has enhanced CH₄ conversion and hence CO₂ conversion. The 5wt % Ce-promoted catalyst showed the highest CH₄ conversion among all the catalysts indicating that increased Ce loadings somewhat yielded superior physicochemical property to Ni/MgO. Most likely, the addition of Ce offers alternative pathway to gasify any deposited carbon species attributed to its excellent redox property, thus ensuring sustainable active area for CH₄ dry reforming. Subsequently, higher amount of CO was yielded (c.f. Figure 4.14) and higher CH₄ conversion was achieved. In addition, as aforementioned, alternative pathway of consuming CH₄ such as CH₄ cracking may also explained the surge in conversion.

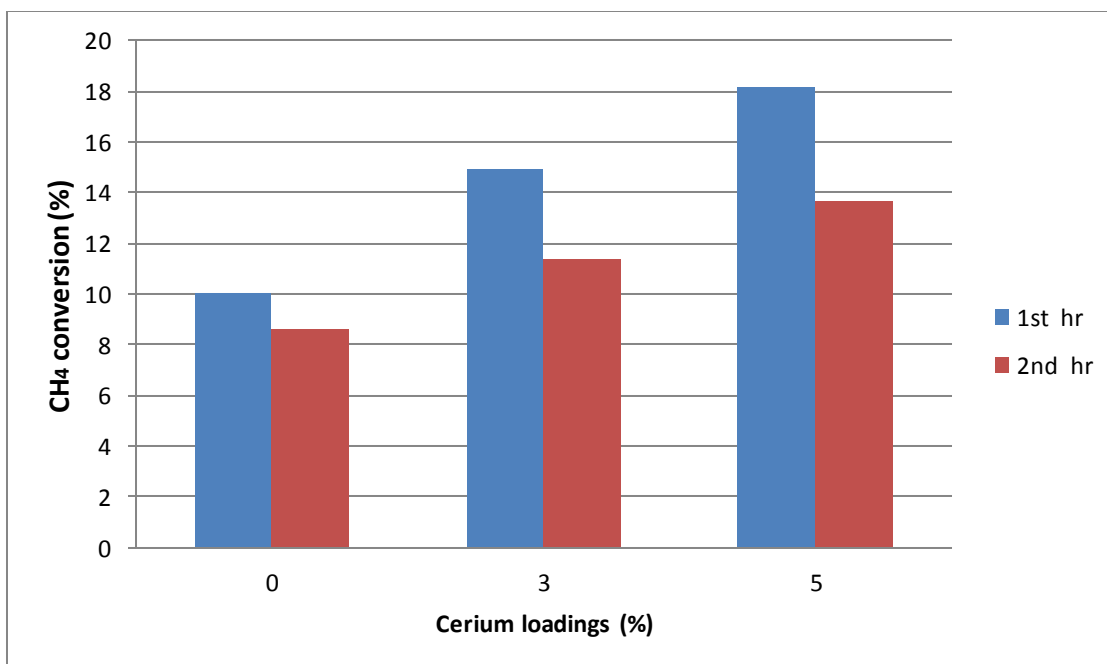


Figure 4.15 CH₄ conversion with various cerium loadings at the first and second hour of the reaction

4.2.2 Effect of Reaction Temperature

From the catalyst screening study, 5wt % Ce-Ni/MgO catalyst has been determined as the best performing catalyst due to the highest conversion attained. Therefore, this catalyst was employed for further reaction studies. The influence of reaction temperature on the reaction rate over 5 wt% Ce-Ni/MgO catalyst was further explored. Figures 4.16 and 4.17 show the variation of rates of formation of CO and H₂ with temperature respectively whilst Figure 4.18 shows the variation of rate of consumption of CH₄ with temperature. The feed stream consisted of 50:50 vol% with a total inlet flow of 100 ml/min. As shown in Figures 4.16 and 4.17, the rates of formation of both CO and H₂ increased with increasing temperature in accordance to the Arrhenius principle. In addition, the rate of consumption of CH₄ also increased when temperature increased as shown in Figure 4.18.

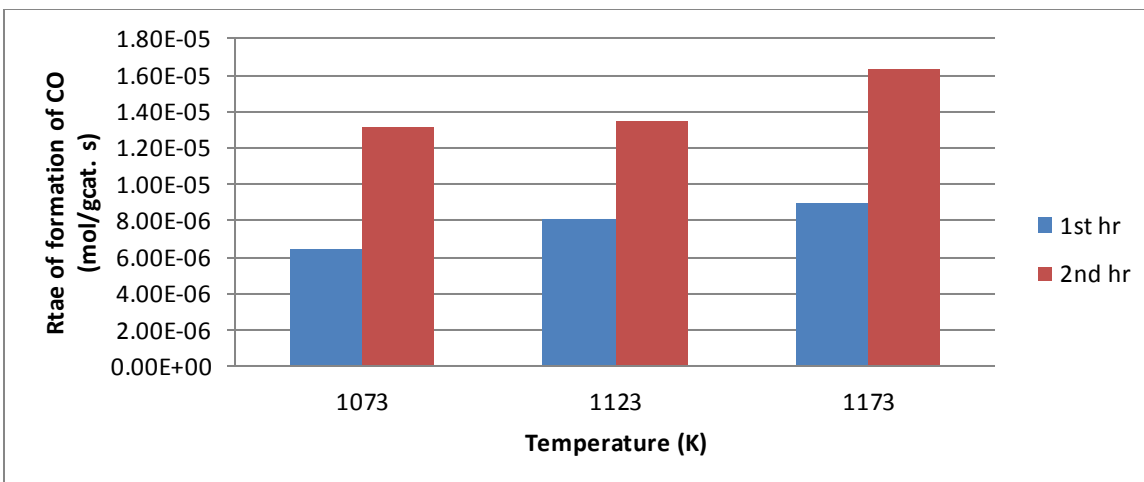


Figure 4.16 Variation of rate of formation of CO with temperature at CH_4/CO_2 ratio = 1:1 at the first and second hour of the reaction

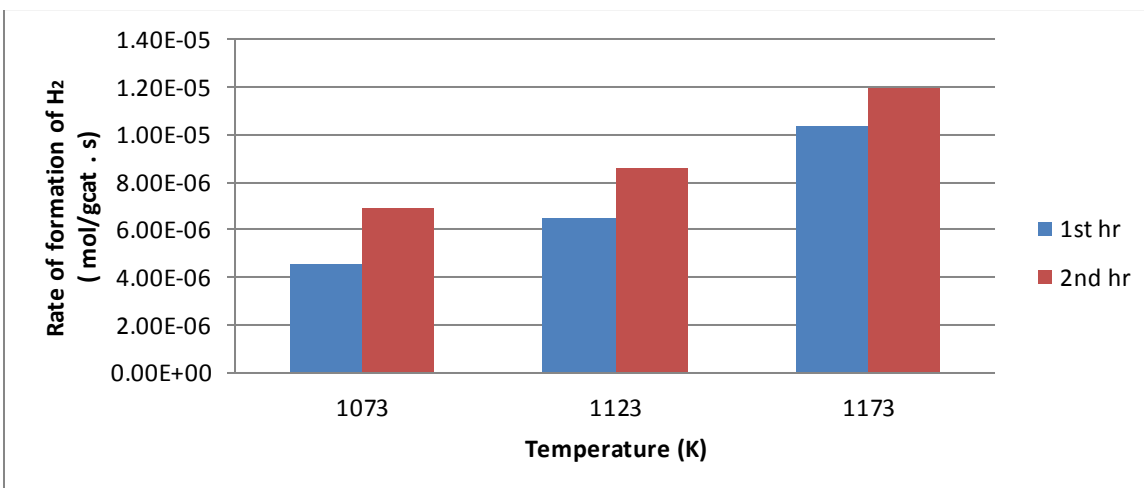


Figure 4.17 Variation of rate of formation of H_2 with temperature at CH_4/CO_2 ratio = 1:1 at the first and second hour of the reaction

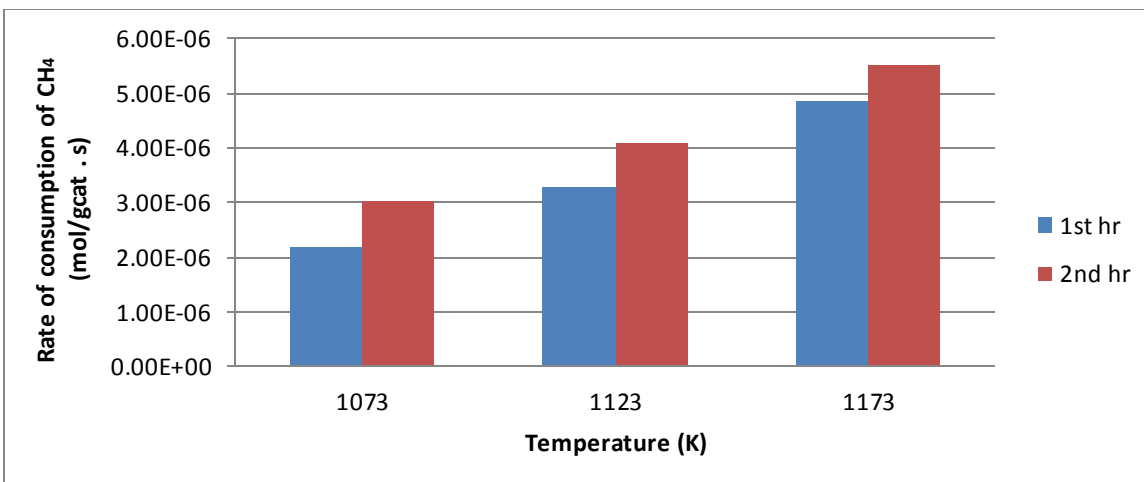


Figure 4.18 Variation of rate of consumption of CH₄ with temperature at CH₄/CO₂ ratio = 1:1 at the first and second hour of the reaction

A plot of $\ln(r)$ versus $1/T$ based on kinetic data collected for the second hour is shown in Figure 4.19. Activation energy was determined from the slope of the best fit. The activation energies for CO formation, H₂ formation and CH₄ consumption were 22.37 kJ/mol, 56.52 kJ/mol and 62.69 kJ/mol respectively.

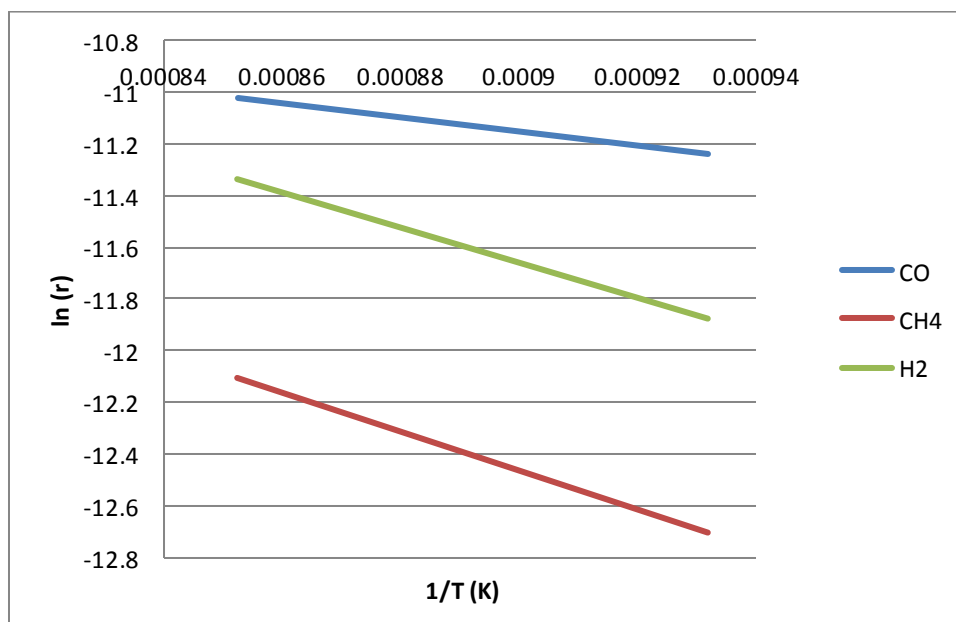


Figure 4.19 Plot of $\ln(r)$ versus $1/T$ for rate of formation of CO, H₂ and rate of consumption of CH₄

4.3 Spent Catalyst Characterization

4.3.1 FESEM Imaging

Figure 4.20 shows the image of coked catalyst of 3wt% Ce-Ni/MgO whereas Figure 4.21 shows the image of coked catalyst of 5wt% Ce-Ni/MgO. No visible filamentous carbon structure was observed for both catalyst as shown in Figures 4.20 and 4.21. In addition, the particle size of fresh and spent 5 wt% Ce-Ni/MgO catalyst was nearly identical (c.f. Figures 4.4 and 4.21). Thus, for 5 wt % Ce-Ni/MgO, the extent of particle sintering was very low and the carbon deposition was not severe.

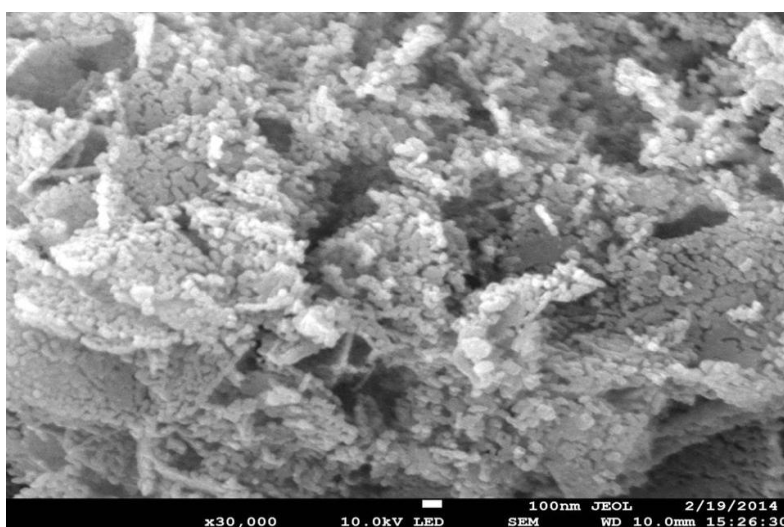


Figure 4.20 SEM image of spent 3 wt% Ce-Ni/MgO catalyst

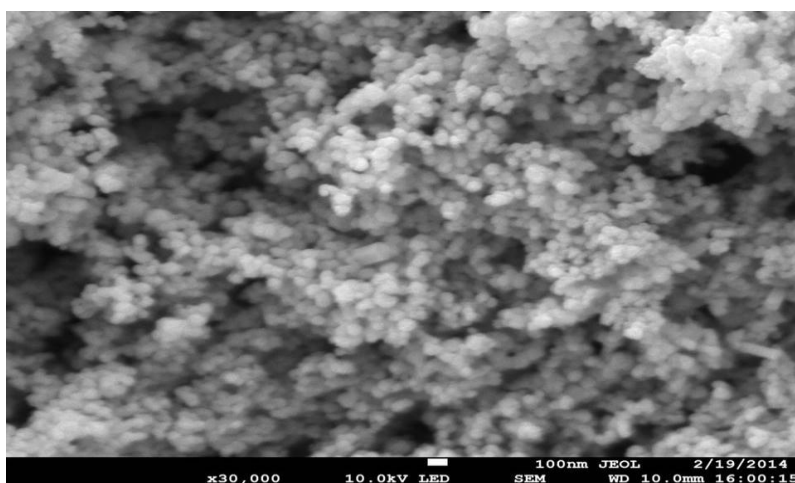


Figure 4.21 SEM image of spent 5wt% Ce-Ni/MgO catalyst

CHAPTER 5 CONCLUSIONS

AND RECOMMENDATIONS

5.1 Conclusions

XRD diffraction patterns of fresh 5wt% Ce-Ni/MgO catalyst showed peaks representing MgO at $2\theta = 37.00^\circ$ and NiO at 42.99° , 62.41° , 74.84° and 78.79° . The peak at 42.99° has sharp intensity indicating that the catalyst has good crystallinity and amorphous phase is not present. From the BET characterization of both fresh 3 wt% and 5 wt% Ce-Ni/MgO catalysts, it can be concluded that the 5 wt% Ce-Ni/MgO catalyst has larger BET specific surface area indicating that the nickel metal is well dispersed on the MgO support even with the increased Ce loadings. In addition, the pore volume and pore diameter of 5 wt% Ce-Ni/MgO catalyst are slightly larger than that of 3 wt% Ce-Ni/MgO catalyst. From FESEM imaging, it can be observed that the metallic particles in 5 wt% Ce-Ni/MgO catalyst are uniformly distributed. From EDX of fresh 5 wt% Ce-Ni/MgO catalyst, only a small amount of carbon is found for the catalyst proving that the catalyst has high carbon removal efficiency.

TGA of Ni/MgO and 5 wt% Ce-Ni/MgO catalysts, showed that at the heating ramp of $10^\circ\text{C}/\text{min}$, 5 wt% Ce-Ni/MgO catalyst gives a slightly higher peak compared to Ni/MgO catalyst showing that promotion of Ce to the catalyst gives a greater extent of decomposition of $\text{Ni}(\text{NO}_3)_2$ into NiO. For the Kissinger model of the two catalysts, it was obvious that 5 wt% Ce-Ni/MgO catalyst has much higher activation energy than Ni/MgO catalyst indicating that 5 wt% Ce-Ni/MgO catalyst is highly stable due to the stronger metal-metal interactions in the catalyst. XP spectra of fresh Ni/MgO catalyst showed deconvolution of Ni2p in three components at 859.98, 868.88 and 877.68 eV, existence of Mg1s at 1307.78 eV and O1s at 534.58 eV. While, XP spectra of fresh 3 wt% Ce-Ni/MgO catalyst showed deconvolution of Ni2p in three components at 860.58, 866.88 and 878.18 eV, existence of Mg1s at 1308.48 eV and O1s at 535.48 e. Other than that, for fresh 3 wt% Ce-Ni/MgO catalyst, Ce3d is found to be deconvoluted at 878.08,

887.18, 903.98 and 921.88 eV. XP spectra of fresh 5 wt% Ce-Ni/MgO catalyst showed the deconvolution of Ni2p in three components at 859.68, 866.08 and 877.08 eV, presence of Mg1s at 1307.38 eV and O1s at 535.48 eV. In addition, main signals of Ce3d are observed at 876.98, 885.78, 902.8 and 920.78 eV.

Reaction studies have found that both 3 wt% and 5 wt% Ce-Ni/MgO catalysts gave almost equal rate of formation of product yield (H₂ and CO) which is greater than that of unpromoted Ni/MgO catalyst at equimolar feed mixture (CH₄ and CO₂) and reaction temperature of 1123K. Moreover, the ratio of H₂ to CO for both 3 wt% and 5 wt% Ce-Ni/MgO catalysts is greater than unity. Therefore, it can be said that Ce not only has improved the reactivity of catalyst, it also provides an alternative pathway that can enhance the H₂:CO ratio, most likely the enhancement of CH₄ cracking to produce more H₂. In addition, 5 wt% Ce-promoted showed the highest CH₄ conversion among all the catalysts indicating that increased Ce loadings somewhat yielded superior physicochemical property to Ni/MgO. The highest CH₄ conversion indicates that addition of Ce offers alternative pathway to gasify any deposited carbon species, thus ensuring sustainable active area for CH₄ dry reforming and yielding higher amount of CO.

The 5wt% Ce-Ni/MgO catalyst was then employed for further reaction studies. The increasing temperature results in increase of the rate of formation of both CO and H₂ as well as the rate of CH₄ consumption. This is in agreement with the Arrhenius principle. The highest rate was achieved at 1173K, but this temperature is not feasible in the industry point of view. A graph of ln(r) versus $\frac{1}{T}$ was plotted for CO formation, H₂ formation and CH₄ consumption. CH₄ consumption showed the highest activation energy which is 62.59 kJ/mol.

From FESEM imaging of used 3 wt% Ce-Ni/MgO and 5wt% Ce-Ni/MgO catalysts, no visible filamentous carbon was observed for both catalysts showing that the carbon deposition was not severe. By comparing both fresh and spent 5 wt% Ce-Ni/MgO catalysts, it can be observed that the particle size was nearly identical indicating that the extent of particle sintering was very low.

5.2 Recommendations

1. Based on the findings and observation of this research project, the following suggestions are proposed for future studies:
2. The effect of pressure of feed mixture on the composition of product yield can be investigated. Varying feed pressure seems to be interesting to study the influence on the composition of product yield.
3. The catalyst should be gasified by H_2/N_2 gas held at 2h in order to activate the catalyst before the reaction started. Products yield may probably increase.
4. Different types of promoters will also influence the catalyst performance. La promoted catalyst is recommended instead of cerium. The different types of promoters employed are encouraged to be further explored.
5. There are various types of carbon deposited on the catalyst. The actual type and its amount formed are essential as this information can be used to undergo further research on the effective methods of coke reduction.
6. FTIR is recommended to determine the species present on the catalyst. It can clearly point out species. Elemental analysis is important in catalysis research.

REFERENCES

Adriana Campos, Josue ´M. Filho and Alcinea C. Oliveira. (2012). Mesoporous catalysts for dry reforming of methane: Correlation between structure and deactivation behavior of Ni-containing catalysts, *international journal of hydrogen energy*, 37, 12281-12291

Agamuthu, P. (1995). Palm oil mill effluent—treatment and utilization. In: Sastry, C.A., Hashim, M.A., Agamuthu, P. (Eds.), *Waste Treatment Plant*. Narosa Publishing House, New Delhi, 338–360.

Aiello, R., Fiscus, J.E., Loye, H.C. and Amiridis, M.D. (2000). Hydrogen production via the direct cracking of methane over Ni/SiO₂: catalyst deactivation and regeneration. *Appl. Catal. A: Gen.*, 192, 227–234.

Albertazzi, S., Arpentinier, P., Basile, F., Del Gallo, P., Fornasari, G., Gary, D. and Vaccari, A. (2003). *Appl. Catal. A*, 247, 1–7.

Alvarez-Galvan, M.C., Navarro, R.M., Rosa, F., Bricen˜ o, Y., Gordillo Alvarez, F. and Fierro, J.L.G. (2008). Performance of La, Ce-modified alumina-supported Pt and Ni catalysts for the oxidative reforming of diesel hydrocarbons. *Int J Hydrogen Energy*, 33, 652–663.

Anderson, J.R. and Pratt, K.C. (1985). *Introduction to characterization and testing of catalyst*. Sydney: Academic Press.

Arif, S. and T.A. Tengku Mohd Ariff. (2001). *The Case Study on the Malaysian Palm Oil*, Paper prepared for the UNCTAD/ESCAP Regional Workshop on Commodity Export Diversification and Poverty Reduction in South and South-East Asia, Bangkok.

Armor, J. N. (1999). The Multiple Roles for Catalysis in the Production of H₂. *Applied Catalysis A: General*, 21, p. 159-176.

Ayabe, S., Omoto, H.; Utaka T., Kikuchi, R., Sasaki, K., Teraoka, Y. and Eguchi, K. Catalytic autothermal reforming of methane and propane over supported metal catalysts, *Appl. Catal. A: Gen.*, 241, 261-269.

Ballarini, A.D., Miguel, S.R., Jablonski, E.L., Scelza, O.A. and Castro A.A. (2005). Reforming of CH₄ with CO₂ on Pt- supported catalysts: Effect of the support on the catalytic behavior. *Catal Today*, 107-108, 481-486.

Barrett, E.P., Joyner, L.G., and Halenda, P.P. (1951). The determination of pore volume and area distributions in porous substances. I. Computations from nitrogen isotherms. *J Amer Chem Soc*, 73, 373-380.

Bartholomew, C.H., Weatherbee, G.D. and Jarvi, G.A. (1980). Effects of carbon deposits on the specific activity of nickel and nickel bimetallic catalysts. *Chem. Eng. Commun.*, 5, 125-134.

Bartholomew, C.H. (2001). Mechanisms of catalyst deactivation. *Appl. Catal. A: Gen.*, 212, 17- 60.

Bell, A.T. (1987). Characterization of carbonaceous residues on catalysts, in : Petersen, E.E. & Bell, A.T. (Eds.) Catalyst Deactivation. Marcel Dekker, Inc., New York and Basel, 235-260.

Becerra A, ME Iriarte, M Dimitrijewits, and A Castro-Luna. 2002. "Promoting effects of rhodium on supported nickel catalysts in the dry reforming of methane." Boetín de la Sociedad Chilena de Químical, 47(4), 385-392.

Bergeret, G. and Gallezot, P. (1997). Particle size and dispersion measurements, in: Ertl,G.,Nozinger, H. & Weitkamp, J(Eds.). Handbook of Heterogeneous Catalysis Weinheim.

Biloen, P., Dautzenberg, F.M. and Sachtler, W.M.H. (1977). Catalytic dehydrogenation of propane to propene over platinum and platinum-gold alloys. J. Catal., 50, 77-86.

Bogner, J., Spokas, K., Burton, E., Sweeney, R. and Corona, V. (1995). Landfills as atmospheric methane sources and sinks. Chemosphere 31 (9), 4119–4130.

Borowiecki, T., Golebiowski, A. and Stasinska, B.(1997). Effects of Small MoO₃ Additions on the Properties of Nickel Catalysts for the Steam Reforming of Hydrocarbons. Appl. Catal. A: Gen., 153, 141-156.

Bouwman, R. and Biloen, P. (1977). Valence state and interaction of platinum and germanium on γ -Al₂O₃ investigated by X-ray photoelectron spectroscopy. J. Catal., 48, 209-216.

Bradford, M.C.J. and Vannice, M.A. (1998). CO₂ reforming of CH₄ over supported Pt catalysts. J. Catal., 173, 157-171.

Bradford, M. and Vannice. M. (1999). Catal. Rev. Sci. Eng, 411- 415.

Bradford, M.C.J. and Vannice, M.A. (1999). "The role of metal-supported interactions in CO₂ reforming of CH₄." Catal. Today, 50, 87-96.

Bradford, M.C.J. and Vannice, M. A. (1996). Catalytic reforming of methane with carbon dioxide over nickel catalysts. I. Catalyst characterization and activity. Appl. Catal. A: Gen., 142, 73- 96.

Brunauer, S.,Emmett P.H. and Teller E. (1938). Adsorption of gases in multimolecular layers. J Amer Chem Soc, 60, 309-319.

Burch, R. and Garla, L.C. (1981). Platinum-tin reforming catalysts: II. Activity and selectivity in hydrocarbon reactions. J.Catal., 71, 360-372.

Burtin, P., Brunelle, J.P. Pijolat, M. and Soustelle, M. (1987). Influence of surface area and additives on the thermal stability of transition alumina catalyst supports: I. Kinetic data. Appl. Catal., 34, 225-238.

Chen, H.W., Wang, C.Y., Yu, C.H., Tseng, L.T. and Liao, P.H. (2004). Catal. Today, 97, 173-180.

- Choudhary, V. R, Uphade, B. S. and Mamman, A. S. (1998). Simultaneous steam and CO₂ reforming of methane to syngas over NiO/MgO/SA-5205 in presence and absence of oxygen, *Appl. Catal. A: Gen.*, 168, 33- 46.
- Christensen, K.O., Chen, D., Lødeng, R., Holmen, A. (2006). *Appl. Catal. A*, 314, 9–22.
- Coq, B. and Figueras, F. (1984). Conversion of methylcyclopentane on platinum-tin reforming catalysts. *J. Catal*, 85, 197-205
- Cullity, B.D. (2001). *Elements of X-ray diffraction*. London: Prentice-Hall International.
- Damyanova, S. and Bueno, J.M.C. (2003). Effect of CeO₂ loading on the surface and catalytic behaviours of CeO₂-Al₂O₃ supported Pt catalysts. *Appl. Catal. A*, 253, 135-150
- Damyanova, S., Pawele, B., Arishtirova, K. and J.L.G. (2011). Fierro. Biogas reforming over bimetallic PdNi catalysts supported on phosphorus-modified alumina. *International Journal of Hydrogen Energy* 36, 10635-10647
- Daza, C.E., Gallego, J., Mondragón, F., Moreno, S. and Molina, R. (2010). High stability of Ce-promoted Ni/Mg–Al catalysts derived from hydrotalcites in dry reforming of methane. *Fuel*, 89, 592–603.
- Dias, J.A. , Assaf, J.M. (2003). *Catal. Today*, 85, 59–68.
- Djaidja, S. Libs, A. Kiennemannb and A. Barama. (2006). Characterization and activity in dry reforming of methane on NiMg/Al and Ni/MgO catalysts. *Catal. Today*, 113, 194-200.
- Dollimore, D. and Heal, G.R. (1964). An improved method for the calculation of pore size distribution from adsorption data. *J Appl. Chem.*, 14, 109-114.
- Dr. F.W. Klaarenbeeksingel. (2009). Literature review and proposals from the RSPO Working Group on Greenhouse Gases: Greenhouse Gas Emissions from Palm Oil Production.
- Erdohelyi, et al. (1994). *Appl. Catal. A: Gen.*, 108 (2) 205.
- Fan, M.S., Zuhairi Abdullah, A., Bhatia, S. (2010). *Appl. Catal. B*, 100, 365–377.
- Faroldi, B.M., Lombardo, E.A. and Cornaglia, L.M. (2011). Ru/La₂O₃–SiO₂ catalysts for hydrogen production in membrane reactors. *Catal. Today*, 172, 209-217
- Farrauto, R.J. and Heck, R.M. (1999). Catalytic converters: state of the art and perspectives. *Catal. Today*, 51, 60-351.
- Fogler, H.S. (1999). *Elements of Chemical Reaction Engineering*. Prentice Hall PTR, New Jersey.

Forzatti, P. and Lietti, L. (1999). Catalyst deactivation. *Catal. Today*, 52, 165-181 G.C.d.
Araujo, et al. (2008). *Catal. Today* 133/135 (0) 129.

Goldwasser, M.R. et al. (2005). *Catal. Today*, 107/108, 106-113.

Gregg, S.J. and Sing, K.S.W. (1982). *Adsorption, Surface Area, and Porosity*. 2nd ed.
London: Academic Press.

Gucbilmez, Y, Dogu, T and Balci, S. Ethylene and acetaldehyde production by selective oxidation of ethanol using mesoporous V-MCM-41 catalyst. *Ind Eng Chem Res* 2006;45: 3496–502.

Guczi, L., Stefler, G., Geszti, O., Sajó, I., Paszti, Z., Tompos, A. and Schay, Z. (2010). Methane dry reforming with CO₂: A study on surface carbon species. *App Catal A: Gen.*, 375, 236-246.

Guo, J.J., Lou, H., Zhu, Y.H. and Zheng, X.M. (2004). Dry reforming of methane over nickel catalysts supported on magnesium aluminate spinels. *App Catal A: Gen.*, 273, 75-82.

Habib, M.A.B., Yusoff, F.M., Phang, S.M. and S. Mohamed. (1997). Nutritional values of chironomid larvae grown in palm oil mill effluent and algal culture. *Aquaculture*, 158, 95-105.

Hickman, D.A. and Schmidt, L.D. (1992). *J. Catal.*, 138, 267-273.

Horiuchi, T., Sakuma, K., Fukui, T., Kubo, Y., Osaki, T. and Mori, T. (1996). Suppression of Carbon Deposition in the CO₂-Reforming of CH₄ by Adding Basic Metal Oxides to a NiO/Al₂O₃ Catalysts, *Appl. Catal. A: Gen.*, 144, 111-120.

Horváth, A., Stefler, G., Geszti, O., Kienneman, A., Pietraszek, A. and Guzzi, L. (2011). *Catal. Today*, 169, 102–111

Istadi, N.A.S. Amin. (2005). Co-generation of C₂ hydrocarbons and synthesis gases from methane and carbon dioxide: a thermodynamic analysis, *J. Nat. Gas Chem*, 14, 140–150.

James, A.L. (2006). Kinetics, catalysis and mechanism of methane steam reforming, 1-118.

Khalid, R. and Wan Mustafa, W.A. (1992). External benefits of environmental regulation: Resource recovery and the utilisation of effluents. *The Environmentalist*, 12, 277-285.

Langmuir, I. (1916). The constitution and fundamental properties of solids and liquids. *J Amer Chem Soc*, 38, 2221-2267.

Larisa A. Arkatovaa, Oleg V. Pakhnutova, Alexandr N. Shmakovb, Yury S. Naiborodenkoc and Nikolai G. Kasatskyc. (2011). Pt-implanted intermetallides as the catalysts for CH₄-CO₂ reforming. *Catal. Today*, 171,156-167.

- Liebhaufsky, H.A., Peiffer, H.G., Winslow, E.H., and Zeman, P.D. (1972). X-ray electrons and analytical chemistry. New York: Wiley-Interscience, John Wiley & Sons Inc.
- Lim, S.K. and Low C.Y.(2013). A retrofitted palm oil mill effluent treatment system for tapping biogas, 5, 106-114.
- Liu, D., Quek, X.Y., Cheo, W.N., Lau, R., Borgna, A. and Yang, Y. (2009). *J. Catal.*, 266, 380–390.
- Ma, A.N. (1999). Treatment of palm oil mill effluent. In: Singh, G., Lim, K.H., Leng, T., David, L.K. (Eds.), *Oil Palm and the Environment: A Malaysian Perspective*. Malaysia Oil Palm Growers Council, Kuala Lumpur, 113–126.
- Ma, A.N. (2000). Environmental Management for the Oil Palm Industry. *Palm Oil Dev.*, 30, 1-10.
- Marturano, M., Aglietti, E.F. and Ferretti, O. (1997). *Mater. Chem. Phys.* 47, 252–256.
- Maxim Lyubovsky, Subir Roychoudhury and Rene LaPierre. (2004). Catalytic partial “oxidation of methane to syngas” at elevated pressures. *Catal. Lett.* , 3–4, 113-114.
- Michler, G.H. (2004). *Electron microscopy of polymers*. Berlin Heidelberg: Springer.
- Mohd Hassan Amin, Kshudiram Mantri, Jarrod Newnham, James Tardio, Suresh K. Bhargava. (2012). Highly stable ytterbium promoted Ni/-Al₂O₃ catalysts for carbon dioxide reforming of methane. *Appl. Catal B: Environ.*, 217-226.
- Moulijn, J. A., van Diepen, A.E. and Kaptejin, F. (2001). Catalyst deactivation: is it predictable? What to do? *Appl. Catal. A: Gen.*, 212, 3-16.
- Muller, A.C., Engelhard, P.A. and Weisang, J.E. (1979). Surface study of platinum-tin bimetallic reforming catalysts. *J. Catal.*, 56, 65-72.
- Nagaoka K, Seshan K, Aika K, Lercher JA. (2001). Carbon deposition during carbon dioxide reforming of methane – comparison between Pt/Al₂O₃ and Pt/ZrO₂. *J. Catal.*, 197, 34–42.
- Palm, C., Cremer, P., Peters, R., Stolten, D.(2002). Small-scale testing of a precious metal catalyst in the autothermal reforming of various hydrocarbon feeds, *Journal of Power Sources*, 106, 231-237.
- Parera, J.M. and Beltramini, J.N. (1988). Stability of bimetallic reforming catalysts. *J. Catal.*, 112, 357-365.
- Peña, M. A., Gómez, J. P. & Fierro, J. L. G. (1996). New Catalytic Routes for Syngas and Hydrogen Production, *Appl Catalysis A: Gen.*, 144, 7-57.
- Pierzynski, G.M., J.T.Sims and G.F. Vance. (2005). *Soils and Environmental Quality*, CRC Press.

- Renshaw, G.D., Roscoe, C. and Walker, P.L. (1971). Disproportionation of CO: II. Over cobalt and nickel single crystals. *J. Catal.*, 22, 394 – 410.
- Richardson, J.T. (1972). Experimental determination of catalyst fouling parameters. *Ind. Eng. Chem. Proc. Des. Dev.*, 11, 12-14.
- Rostrup-Nielsen, J. R. (1984). Catalytic Steam Reforming. In: *Catalysis, Science and Technology* (Anderson, J. R.; Boudart, M., eds.), Springer Verlag, Berlin, chapter 1, vol. 5, 1-117.
- Rostrup-Nielsen, J.R., Sehested J, Norskov J.K. (2002). Hydrogen and synthesis gas by steam and CO₂ reforming. *Adv Catal*, 47, 65-74.
- Ruckenstein, E. and Hu, Y. (1995). Carbon dioxide reforming of methane over nickel/alkaline earth metal oxide catalysts, *Appl. Catal. A: Gen.*, 133, 149-161.
- Saman Zafar. (2013). Properties and Uses of POME. *Industrial Waste Management, Southeast Asia*
- Sethupathi,S. (2004). Removal of residue oil from palm oil mill effluent (POME) using chitosan, *Universiti Sains Malaysia*.
- Seyma Ozkara-Aydınoğlu, Emrah Ozensoy and A. Erhan Aksoylu. (2009). The effect of impregnation strategy on methane dry reforming activity of Ce promoted Pt/ZrO₂, *International Journal of Hydrogen Energy*, 34, 9711–9722.
- Shishido, T., Sukenobu, M., Morioka, H., Furukawa, R., Shirahase, H. and Takehira, K. (2001). *Catal. Lett.*, 73, 21-34.
- Sinfelt, J.H. (1979). US Patent, 3 953 368.
- Sing, K.S.W., Everett, D.H., Haul, R.A.W., Moscou,L., Pierotti,R.A., Rouquero,J., and Siemieniewska, T. (1985).Reporting Physisorption Data for Gas Solid Systems with Special Reference to the Determination of Surface Area and Porosity (Recommendations 1984).*Pure Appl. Chem.*, 57, 603-619.
- Sing, K.S.W. and Rouquero, J. (1997). Surface Area and Porosity, in *Handbook of heterogeneous catalysis*, VCH Verlagsgesellschaft mbH: Weinheim.
- Stagg-Williams, S.M., Noronha F.B., Fendley G. and Resasco D.E. (2000). CO₂ reforming of CH₄ over Pt/ZrO₂ catalysts promoted with La and Ce oxides. *J Catal*, 194, 9-240.
- Thermo Nicolet Corporation. (2001). Introduction of Fourier Transform Infrared Spectrometry.1-8.
- Tsyganok, A.I., et al. (2004). *Appl. Catal. A: Gen.*, 275, 149-152.

Wang, H.Y., Ruckenstein, E. (2000). Carbon dioxide reforming of methane to synthesis gas over supported rhodium catalysts: the effect of support. *Appl. Catal. A*, 204, 143–525.

Wang, X., Wang Li, M.M., Wang, H., Li, S., Wang, S. and Ma, X. (2009). Thermodynamic analysis of glycerol dry reforming for hydrogen and synthesis gas production, *Fuel* 88, 2148–2153.

Warren, B.E. (1969). *X-ray Diffraction*. Reading: Addison-Wesley.

Wijbrans and Van Zutphen. (2005). Environmental impact study for the combustion of palm fatty acid distillate in a power plant. Zwolle (the Netherlands).

Wu, T.Y., Mohammad, A. W., Tahim, J.M., & Anuar, N. (2010). Pollution control technologies for the treatment of palm oil mill effluent (POME) through end-of-pipe processes. *J. Environ. Manage.*, 91, 1467–1490.

Xu, B.Q, Wei, J.M., Wang, H.Y., Sun, K.Q. and Zhu, Q.M. (2001). Nano-MgO: novel preparation and application as support of Ni catalyst for CO₂ reforming of methane. *Catal. Today*, 68, 217–256.

Yacob, S., Hassan, M. A., Shirai, Y., Wakisaka, M. and Subash, S. (2005). Baseline study of methane emission from open digesting tanks of palm oil mill effluent treatment. *Chemosphere*, 59, 1575–1581.

Hu, Y. and Ruckenstein, E. (2009). High resolution transmission electron microscopy study of carbon deposited on the NiO /MgO solid solution catalysts, *J. Catal.*, 184, 298–302.

Yang, R., Xing, C., Lv, C., Shi, L. and Tsubaki, N. (2010). *Appl. Catal. A*, 385, 92–100

Junke, X., Wei, Z., Jihui, W., Zhaojing, L., Jianxin, M., Chin, J. (2009). *J. Catal.*, 30, 1076–1084

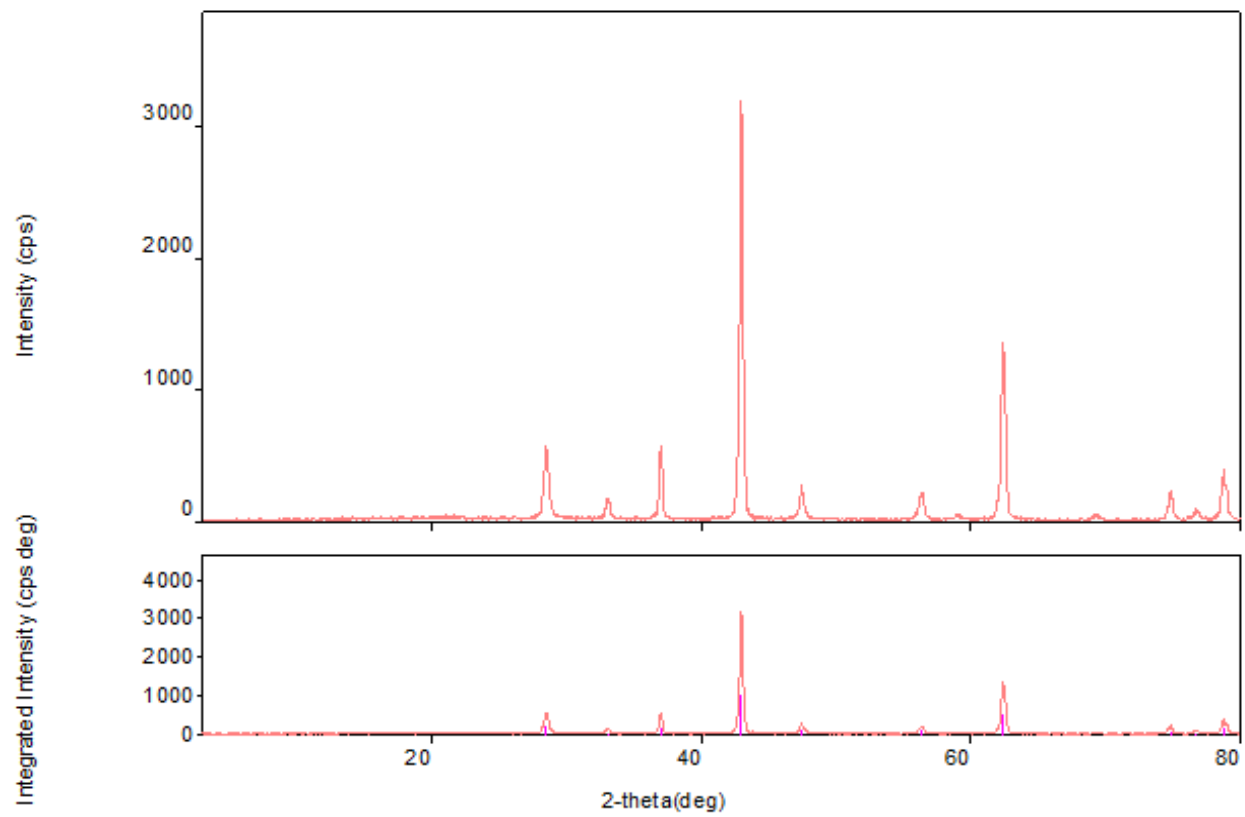
Zhang, B.S. Liu, C. Zhu, Y.L. Tian. (2005). *Appl. Catal. A*, 292, 138–143.

Zhang, T., Amiridis, M.D. Hydrogen production via the direct cracking of methane over silica-supported nickel catalysts. *Appl. Catal. A: Gen.*, 167, 72–161.

APPENDICES

Appendices A

5 wt% Ce-Ni/MgO catalyst

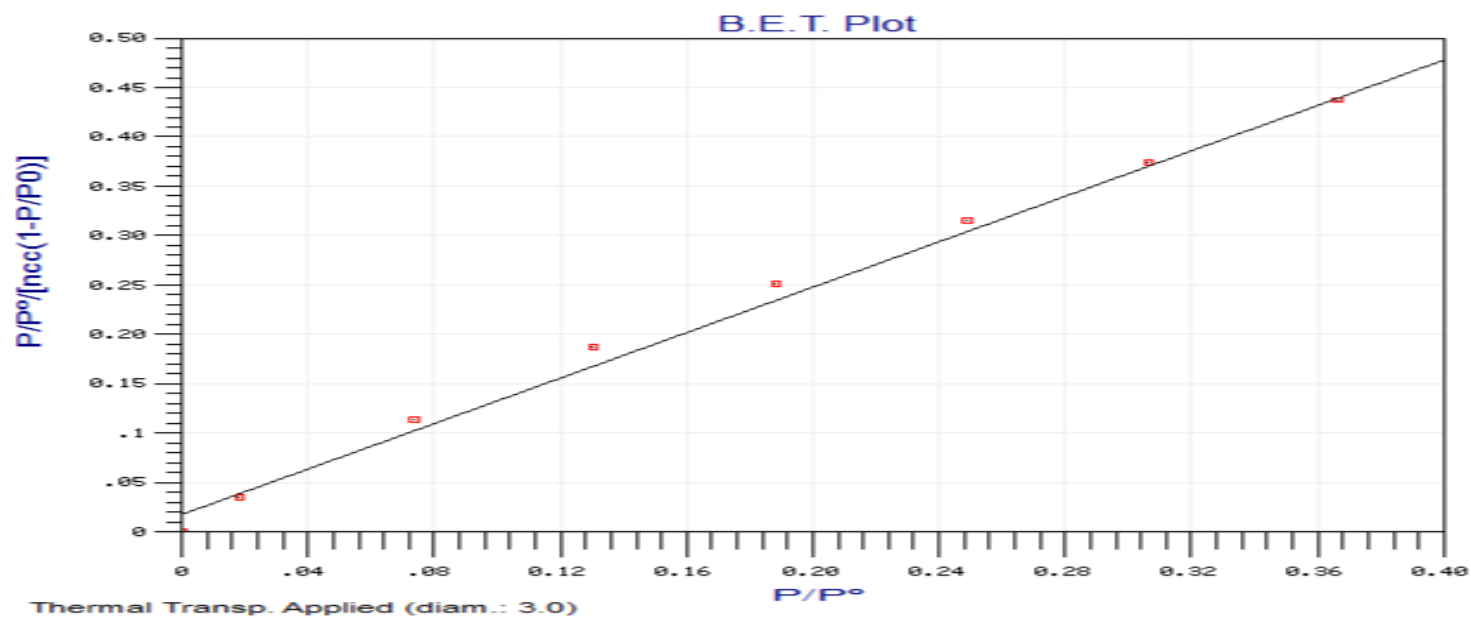


Peak list

2-theta (deg)	d (ang.)	Height(cps)	Int. I(cps*deg)	FWHM(deg)	Size	Phase name
28.531(10)	3.1259(10)	359(19)	172(2)	0.353(8)	242(5)	Unknown,
33.053(19)	2.7079(15)	93(10)	40.9(14)	0.367(15)	236(10)	Unknown,
36.997(9)	2.4277(6)	415(20)	113.8(16)	0.204(8)	429(17)	Unknown,
42.987(5)	2.1023(2)	2443(49)	693(5)	0.214(4)	417(8)	Unknown,
47.457(16)	1.9142(6)	183(14)	93.2(15)	0.373(12)	243(8)	Unknown,
56.36(2)	1.6311(6)	147(12)	75.3(15)	0.37(2)	256(15)	Unknown,
59.06(7)	1.5627(16)	21(5)	11.3(12)	0.51(5)	186(18)	Unknown,
62.407(5)	1.48681(11)	1126(34)	370(3)	0.244(6)	398(9)	Unknown,
74.836(14)	1.2677(2)	163(13)	64.0(14)	0.315(15)	331(16)	Unknown,
76.76(4)	1.2407(6)	42(6)	19.7(13)	0.44(3)	241(19)	Unknown,
78.786(7)	1.21373(9)	300(17)	117.5(19)	0.290(9)	370(11)	Unknown,

Appendices B

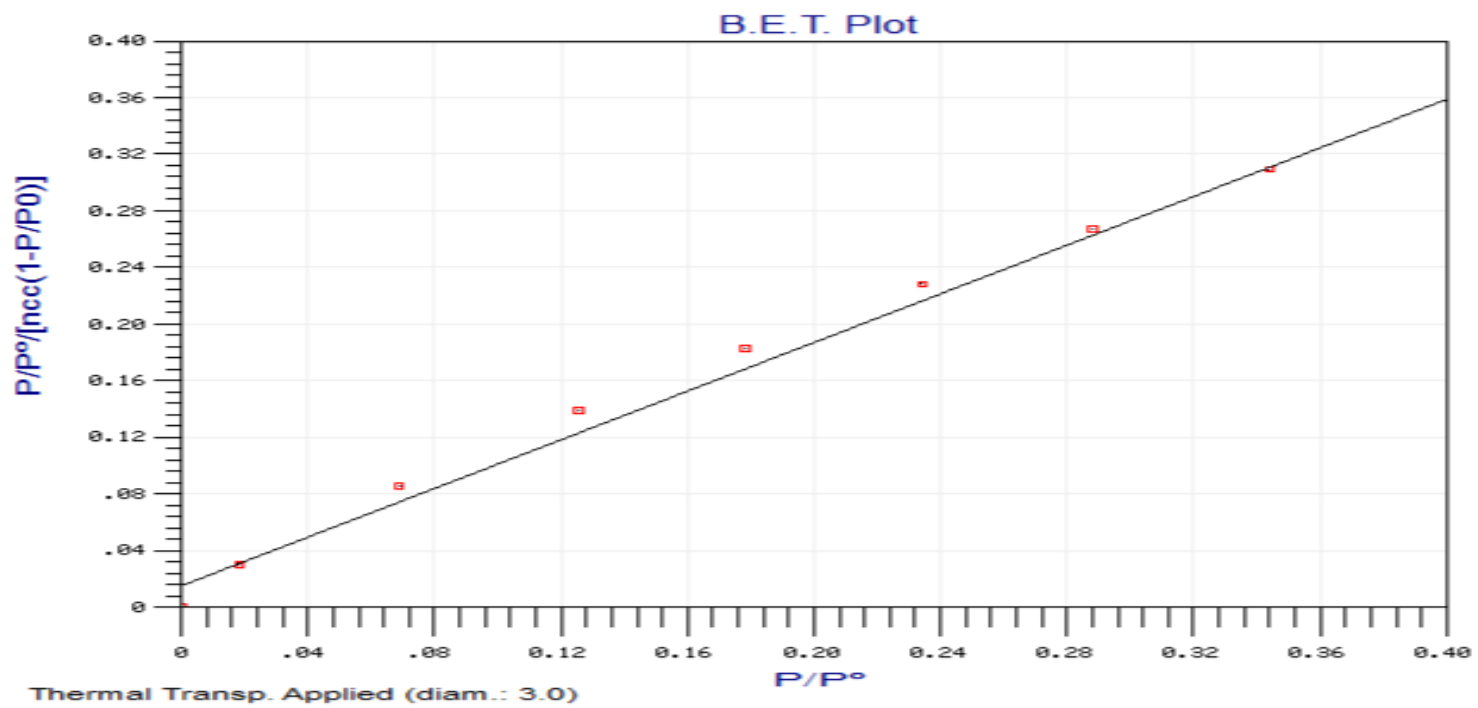
i) 3 wt % Ce-Ni/MgO catalyst



Surface Area calculation results

Calculation Method: B.E.T.
Initial-Final P/P^0 : 0 - .4
Monolayer Volume (ncc/g): .8541248
Specific Surface Area (m^2/g): 10.59064
C Value of BET Equation: 69.97855
Correlation Factor: .9970396

ii) 5 wt% Ce-Ni/MgO catalyst

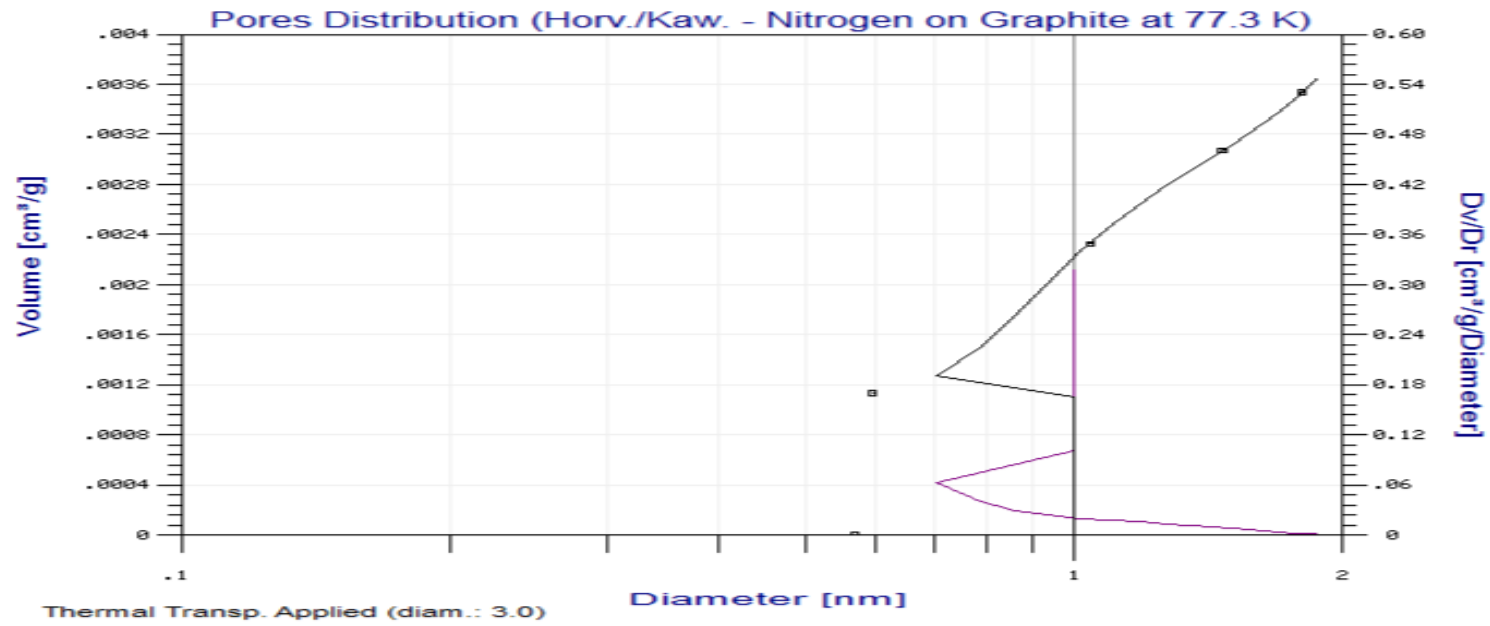


Surface Area calculation results

Calculation Method: B.E.T.
Initial-Final P/P₀: 0 - .4
Monolayer Volume (ncc/g): 1.142086
Specific Surface Area (m²/g): 13.99765
C Value of BET Equation: 58.2858
Correlation Factor: .995577

Appendices C

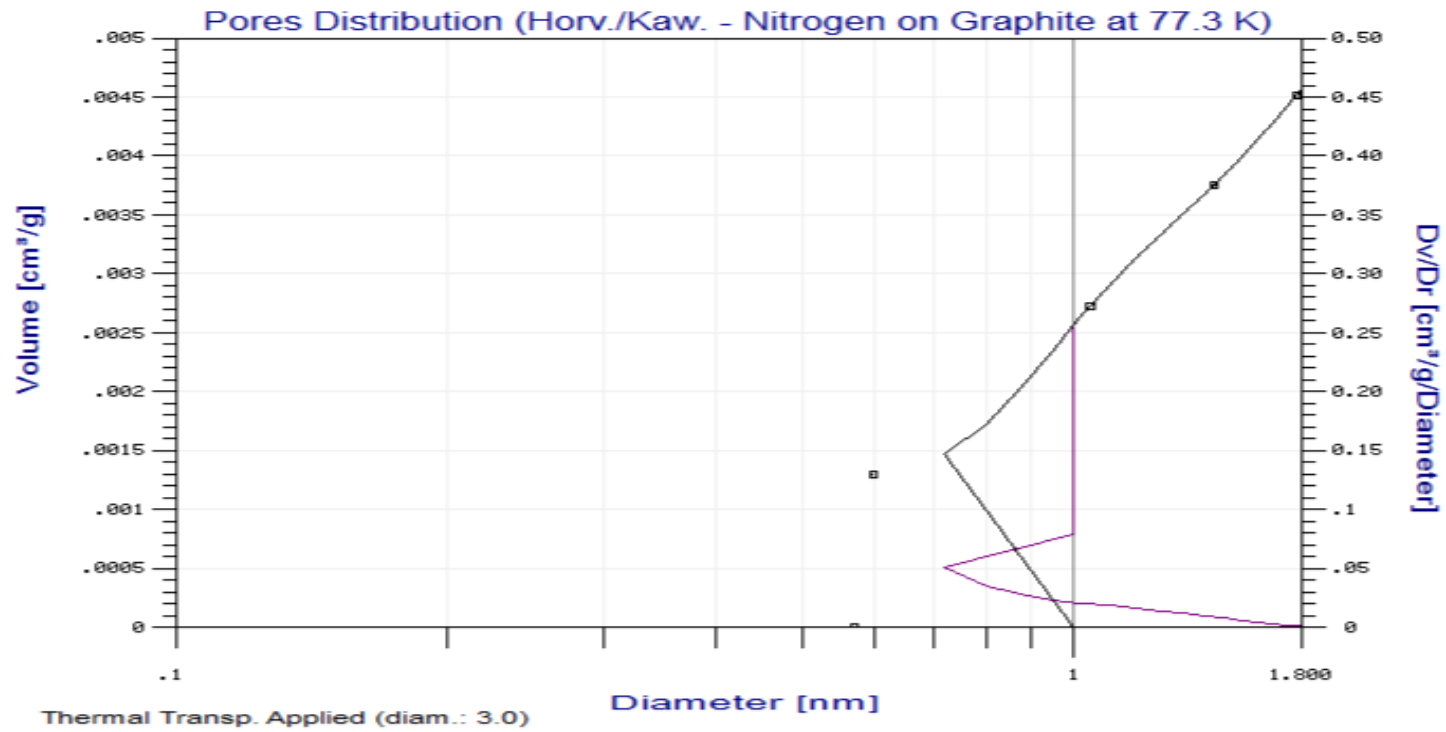
i) 3 wt% Ce-Ni/MgO catalyst



Pore size results

Calculation method: Horvat & Kavazoe
Model: Nitrogen on Graphite at 77.3 K
Pore Size Range (Diameter): 0.0 - 0.15
Cumulative Volume (cm³/g): 0.0035
Maximum Diameter (nm): .5953743
Average Diameter (nm): .8847383

ii) 5 wt % Ce-Ni/MgO catalyst



Pore size results

Calculation method: Horvat & Kavazoe
Model: Nitrogen on Graphite at 77.3 K
Pore Size Range (Diameter): 0.0 - 0.15
Cumulative Volume (cm³/g): 0.0045
Maximum Diameter (nm): .5987141
Average Diameter (nm): .96458

Appendices D

